# *Cut Optimization for Feasibility study of Dark Matter in Di-leptons Final state and Qualification of Silicon Sensors for CMS Phase 2 Upgrade*


**By**

**Samiullah Khan**

**02182113038**

**Department of Physics**

Quaid-i-Azam University

Islamabad, Pakistan

*A DISSERTATION SUBMITTED IN THE PARTIAL FULFILLMENT OF THE REQUIREMENTS FOR THE DEGREE OF MASTER OF PHILOSOPHY.*

(2021-2023)

# Declaration

I, Samiullah Khan (02182113038), solemnly affirm that the work presented in this thesis has been independently produced by me within the designated study period. I further declare that all materials utilized in this thesis, except where appropriately referenced, are my original work and that any instances of plagiarism fall within acceptable limits. I am fully aware that any violation of research regulations set forth by the Higher Education Commission (HEC) may result in disciplinary action as per the prescribed plagiarism guidelines.

Date:01/09/2023

Signature of Student
Samiullah Khan
02182113038

# Certification

I have carefully read and approved of the thesis titled "**Cut Optimization for Feasibility study of Dark Matter in Di-leptons Final state and Qualification of Silicon Sensors for CMS Phase 2 Upgrade**" by **Samiullah Khan** Reg no. 02182113038. I recommend this thesis to the physics department for acceptance, as it fulfills the requirements for the degree of **Master of Philosophy**.

Date: 01/09/2023

**Supervisor:**

Dr. Ashfaq Ahmad
Director EHEPD
National Center For Physics
Quaid-i-Azam University
Islamabad.

**Submitted through:**

Head of Department
Dr. Kashif Sabeeh
Department of Physics
Quaid-i-Azam University
Islamabad.

***This thesis is dedicated to my loving and unwavering parents who have continuously supported and encouraged me through my academic journey with boundless love and unwavering belief in my abilities,***

***Thank you, Dad***

# Acknowledgments

All praise and thanks to Almighty Allah for granting me the opportunity to successfully complete my research project. Darud-o-salam to the last prophet of Allah Hazrat Muhammad (PBUH), who is sent as a mercy to all creation and whom the whole universe has existed for.
I would like to convey my deep gratitude and inspiration to my research supervisor, Dr. ASHFAQ AHMAD, Director of EHEP, NCP Islamabad. His constant encouragement, unwavering guidance, and belief in my abilities have motivated me to go beyond what I thought was possible. Working under his supervision has been a great privilege, and I credit him entirely for providing the right direction and support whenever I needed it. His open-door policy and approachability for research discussions were immensely valuable.
I want to express my profound gratitude to my parents for their unwavering love and support. I am also grateful to my brothers Sanaullah Khan and saadullah Khan, and especially my sisters, who consistently prayed for my success and a better future. Additionally, I extend special thanks to Dr. Saleh, Dr. Wajid, Dr. Gul for their invaluable guidance and assistance.

Samiullah Khan

# Abstract

Standard Model lacks Dark Matter candidates, and hence, we need physics beyond Standard Model. WIMPs (Weakly Interacting Massive Particles) are proposed as potential candidates for Dark Matter by theories beyond the Standard Model. The production of WIMP pairs can be studied in collider experiments. In this thesis, we focus on two topics:

In the first part of my thesis, I concentrated on investigating the cut optimization for feasibility study of Dark Matter in Di-leptons final state. This exploration involved various avenues, with particular emphasis on the mono-Z channel. It involves the creation of a Higgs boson from the fusion of gluons (g g). This Higgs boson then undergoes a series of transformations, eventually giving rise to Z boson and a pseudoscalar particle referred to as "a". The Z boson further decays into oppositely charged leptons, while the pseudoscalar "a" transforms into Dark Matter candidates. For the investigation of this process, we utilized the $MadGraph5\_aMC@NLO$ event generator to simulate collisions between protons at an energy of 13.6 TeV. To better understand this, I employed different criteria to distinguish between the desired signal and the background noise. This involved analyzing essential kinematic factors, including missing transverse energy ($E_T^{miss}$), angular separations ($\Delta\phi$), ($\Delta R$) and invariant mass (M). I also find the significance of each variable. Towards the end, I assessed the overall significance by applying final criteria. This was followed by the computation of the signal significance using the formula $S/\sqrt{B}$. The outcome yielded a signal significance value of $0.45\sigma$.

In the second part of my thesis, I executed measurements using SQC setup at NCP for phase-2 upgrade. This study entailed an analysis of eight key parameters, categorized into global and strip parameters. The global parameters centered on two critical aspects: the relationship between leakage current and reverse bias voltage (IV), as well as the correlation between bulk capacitance and reverse bias voltage (CV). The data acquisition involved varying voltage levels, spanning from 0 to 1000 V for leakage current and 0 to 600 V for bulk capacitance. Meanwhile, the strip parameters encompassed coupling capacitance (CC), interstrip capacitance ($C_{int}$),

strip current ($I_{strip}$), polysilicon resistance ($R_{poly}$), interstrip resistance ($R_{int}$), and dielectric current ($I_{diel}$). For the specific batch identified as 43264_2$S$_035, the resultant average values were as follows: a full depletion voltage of 228 V, a polysilicon resistance of 1.45 MΩ, a coupling capacitance of 137.33 pF, and a strip current of −50.72 pA. These measurements are within specification as laid down down by CMS [1].

# Contents

# List of Figures

# List of Tables

Chapter 1

# Standard Model of Particle Physics

## 1.1 Historical Background

About 400 B.C, Greek philosophers believed matter is made up of atoms. However, we know that the atom is not a fundamental particle. Over time, technology evolved and the discovery of new particles resulted in elementary particle physics. The journey into elementary particle physics began when $e^-$ was discovered by J.J. Thomson. The year 1897 marked his contribution. Thomson discovered electrons in the cathode ray tube, he explains that magnet has the ability to deflect specific rays emitted from the cathode in the cathode ray tube, hence these rays have some charge. Later he measured the charge to mass ratio of the electron. In 1911, Rutherford and his co-workers while performing their experiment on Gold foil discovered that there exists a small dense matter inside the atom from which some of the alpha rays are deflected at various angles, he called it nucleus.It showed that electrons revolve around the nucleus in circular orbits like the planetary system. Later in 1919, he also discovered proton. In 1932, another scientist James Chadwick discovered electrically neutral particle called which he called neutron. It has almost the same mass as that of a proton. This was considered almost the final recipe for the structure of an atom. It explains how fundamental particles of matter interact, including electromagnetic, weak, and strong forces, but not gravity. In 1957, Chien-Shiung Wu demonstrated that weak interactions have no parity conservation [27]. In 1961, Sheldon Glashow and Abdus Salam unified electromagnetic and low-energy interactions. Then Martin Perl discovered the tau in the 1970s at the Stanford Linear Accelerator Center in California. The Z boson is a neutral weak gauge boson discovered by physicists at CERN's Super Proton Synchrotron in 1983. Top quark was discovered at Fermi lab in April 1995. In 2012, the

Large Hadron Collider (LHC) identified the Higgs boson with a mass of 125.35 GeV using the Brout-Englert mechanism [28].

## 1.2 Fundamental Particles in Standard Model

A particle may be classified as either a Boson or a Fermion. Fermions are those particles which obey the Pauli exclusion principle.

### 1.2.1 Leptons

Due to their lack of color charge, leptons and anti-leptons do not participate in strong interactions. As spin 1/2 particles, they come in three generations. First generation quarks include the electron and its neutrino. The second generation includes the muon and their neutrino, and the third generation includes the tau and his neutrino. It's known that neutrinos are chargeless, but have a very small mass due to neutrino oscillation. By Donut collaboration in 2000, tau neutrino was discovered [29]. All neutrinos exhibit left-handedness, while their antiparticles possess opposite characteristics. Their opposite lepton number signs and helicity distinguish them from neutrinos. Leptons participate in electromagnetic, weak, and gravitational interactions. The lepton number conservation is the basic law for the reaction to be allowed. Figure **??** summarizes the key properties of Lepton and antilepton.

**Table 1.1:** Properties of Leptons and their Neutrinos

| Leptons | Symbol | Antiparticle | Charge | Mass (MeV/$c^2$) |
|---|---|---|---|---|
| Electron | $e^-$ | Positron ($e^+$) | $-1$ | 0.511 |
| Muon | $\mu^-$ | Antimuon ($\mu^+$) | $-1$ | $105.7 \times 10^3$ |
| Tau | $\tau^-$ | Antitau ($\tau^+$) | $-1$ | $1776.86 \times 10^3$ |
| Electron Neutrino | $\nu_e$ | Electron Antineutrino ($\bar{\nu}_e$) | 0 | $< 2.2$ |
| Muon Neutrino | $\nu_\mu$ | Muon Antineutrino ($\bar{\nu}_\mu$) | 0 | $< 0.17$ |
| Tau Neutrino | $\nu_\tau$ | Tau Antineutrino ($\bar{\nu}_\tau$) | 0 | $< 15.5$ |

### 1.2.2 Quarks

Quarks and antiquarks have color charges, so that's the reason they participate in strong interaction. As per the standard model, quarks come in three generations. Up (u) and down

(d) quarks are first generation. Charm (c) and strange (s) quarks make second generation spin. Strangeness conservation is not observed in weak interactions, particularly when third-generation particles like top (t) and bottom (b) quarks are involved. Top, up, and charm quarks have a charge of $\frac{2}{3}e$ and antiparticles have opposite charge. Bottom, down and strange quarks has a charge of $-\frac{1}{3}e$ and antiparticles have an opposite charge. In table 1.2, six quarks are listed. Quarks are combined in a manner that results in color neutrality, leading to their classification as hadrons.

**Table 1.2:** Properties of Quarks

| **Quarks** | **Baryon number** | **Strangeness** |
|---|---|---|
| **u** | $\frac{1}{3}$ | 0 |
| **d** | $\frac{1}{3}$ | 0 |
| **c** | $\frac{1}{3}$ | 0 |
| **s** | $\frac{1}{3}$ | -1 |
| **t** | $\frac{1}{3}$ | 0 |
| **b** | $\frac{1}{3}$ | 0 |

### 1.2.3 Bosons

A boson is a particle with integer spin and obeys Bose-Einstein statistics, which explains how electromagnetic, strong, and weak forces interact. Bosons are further categorized as Gauge bosons and Scalar bosons.

#### Gauge Bosons

Gauge bosons have spin 1. There are three types of mediators, which are as follows:

**1**. The mediator responsible for the electromagnetic interaction is referred to as a photon, symbolized by $\gamma$.

**2**. In weak interactions, the mediator is called an intermediate vector boson and their symbols are W and Z.

**3**. In strong interactions, the mediator is called a gluon and its symbol is g.

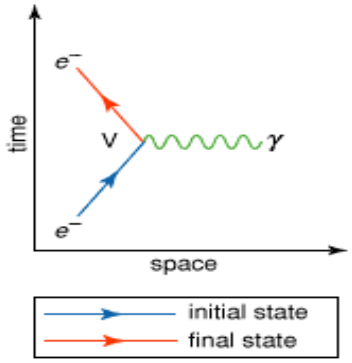


**Figure 1.1:** QED interaction [2].

### Scalar Bosons

Scalar bosons are a type of subatomic particle that are associated with a type of field known as a scalar field. These particles are characterized by a spin of zero and their own antiparticles. The Higgs boson is a scalar particle with a mass of about 125 GeV in the Standard Model.

## 1.3 Fundamental interaction

Nature has four fundamental forces: electromagnetic, weak, strong, and gravitational. The strength of strong, electromagnetic, weak and gravitational interactions are 10, $10^{-2}$, $10^{-13}$, $10^{-42}$ respectively. Figure **??** summarizes the key properties of four fundamental forces.

**Table 1.3:** Properties of Gauge Bosons

| Gauge Bosons | Spin | Charge | Mass | Associated Force |
|---|---|---|---|---|
| Photon ($\gamma$) | 1 | 0 | 0 | Electromagnetic |
| W Boson (W) | 1 | $\pm 1$ | 80.4 GeV/$c^2$ | Weak |
| Z Boson (Z) | 1 | 0 | 91.2 GeV/$c^2$ | Weak |
| Gluon (g) | 1 | 0 | 0 | Strong |
| Graviton (G) | 2 | 0 | 0 | Gravitational |

Most people believe gravity is too weak for its role to be demonstrated. In quantum electrodynamics (QED), the photon serves as a mediator for electromagnetic interactions rather than being involved in mediating gravity. In figure 1.1, as an electron engages in electromagnetic interaction, it has the potential to emit or absorb a photon before transitioning out of the inter-

action. Figure 1.2 illustrates the Coulomb repulsion between two electrons, which is facilitated by the exchange of photons. This phenomenon is termed as Moller scattering.

$e^- + e^- \rightarrow e^- + e^-$

Figure 1.2 also shows the Coulomb attraction of electrons and positrons mediated by the exchange of photons. This process is called Bhabha scattering.

$e^+ + e^- \rightarrow e^- + e^+$

In the right-hand diagram of Figure 1.2, the illustration represents Compton scattering. This is a process where a photon interacts with an electron, resulting in the emission of some of the photon's energy. This interaction can be described as $(e^- + \gamma \rightarrow \gamma + e^-)$.

The physical theory which explains strong interaction is called Quantum chromodynamics [30]. The mediator between two quarks in a strong interaction is called a gluon. Gluon carries dual-color, i-e color and anti-color. The color of the quark may vary during the process q → q + g. A blue up-quark, for example, could become a red up-quark by conversion. As shown in Figure 1.3 (left), colour (like charge) is always conserved, so the gluon must carry the difference away in this case. As a result of the quark color charges, three distinct colors are displayed, namely "red", "blue", and "green". There are $3 \times 3 = 9$ possibilities here, but because of linear combination of red + green + blue, there are 8 different types of gluons exists. Gluons carry

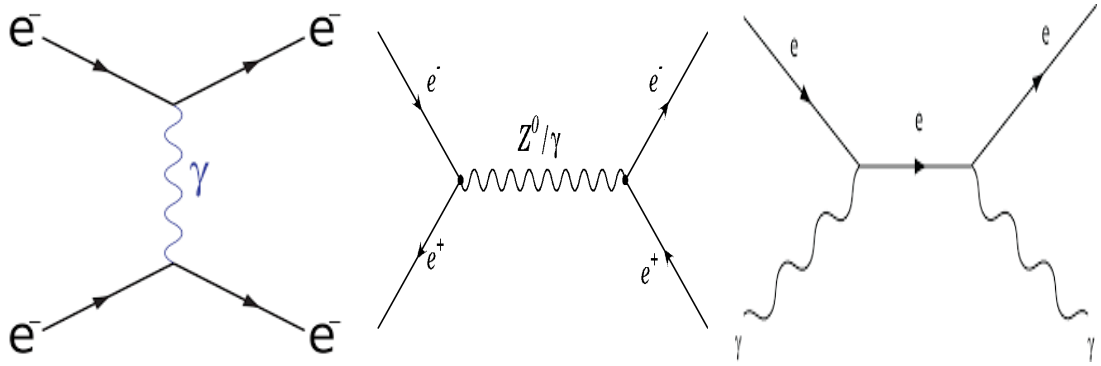


**Figure 1.2:** The left diagram show Moller scattering, center diagrarm show Bhabba scattering and right diagram show Compton scattering [3].

color, unlike photons, that's the reason they directly couple with other gluons. The middle and right side diagram of figure 1.3 shows gluon gluon interaction. The origin of asymptotic freedom is due to decreasing QCD coupling at a short distance. The theoretical framework that elucidates weak nuclear interactions is referred to as Flavor Dynamics (Fritzsch, 1977). Weak interactions do not conserve CP, Parity, and Strangeness properties. W bosons mediates charge interactions, while Z bosons mediate neutral interactions, figure 1.4 explains this distinction.

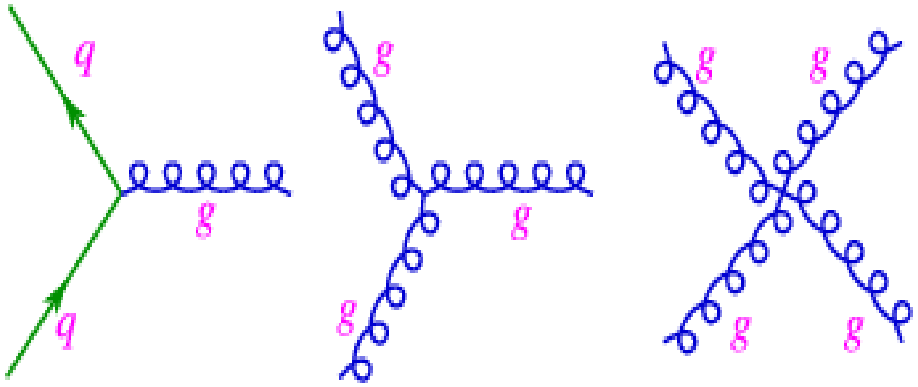


**Figure 1.3:** The left diagram shows the interaction of quarks in QCD , middle and right diagram shows gluon gluon interaction [4].

Figure 1.4 shows a negative lepton is converted into a corresponding neutrino by emitting $w^+$ boson: $(l^- \rightarrow w^+ + \nu_l)$.

Figure 1.4 is shown for: $(e^- + \nu_e \rightarrow e^- + \nu_e)$. In the left diagram of Figure 1.4, a lepton can

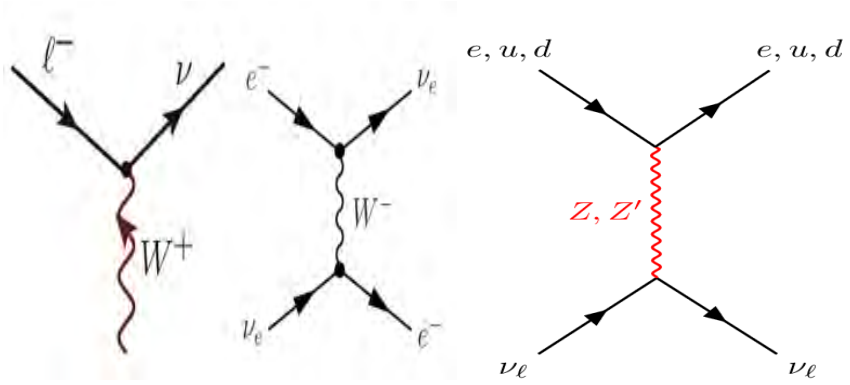


**Figure 1.4:** Feynman diagram in weak interaction for $W^+$, $W^-$ and Z boson [5].

transform into a different lepton through the emission of a Z boson $(l \rightarrow l + Z)$. The center diagram in Figure 1.4 depicts the process where a $W^-$ boson emission transforms a neutrino $(v_\mu)$ and an electron $(e)$ into a neutrino $(v_\mu)$ and an electron $(e)$: $v_\mu + e \rightarrow v_\mu + e$.

Chapter 2

# Large Hadron Collider and CMS Detector

The world's largest particle accelerator, called the Large Hadron Collider, was introduced in 1983. This was a significant year for scientific advancement, several crucial breakthroughs occurred. These include the identification of W and Z bosons, the pioneering achievement of generating antihydrogen atoms in 1995, and, more recently, the landmark detection of the Higgs boson with a mass of 125 GeV/c² [31]. There is a description of the LHC experiment and the CMS experiment in the following section, as well as its phase-2 upgrade.

## 2.1 Large Hadron Collider

Large Hadron Colliders (LHC) are the world's largest particle accelerators. Synchrotron storage rings represent the last phase of a robust accelerator complex that is constructed in the underground cave of the former Large Electron Positron Collider (LEP).

The LHC is designed so that lead nuclei (Pb-Pb) are accelerated at the 5.36 TeV center-of-mass per nucleon, which is denoted as $\sqrt{s}$ for one month every year. In addition to CMS, ATLAS, and LHCb, ALICE includes four major detectors at LHC, located at four places where opposing proton beams collide as in figure 2.1. As a general-purpose detector, ATLAS and CMS are used to measure a wide range of particles created in LHC collisions to find new physics. The LHCb experiment examines CP violations. As part of ALICE, quark gluon plasma is studied in heavy ion collisions. Protons are filled into the two counter-rotating beams of the LHC in bunches. One bunch contain $10^{12}$ protons. There are 2808 bunches in each beam. The proton bunches

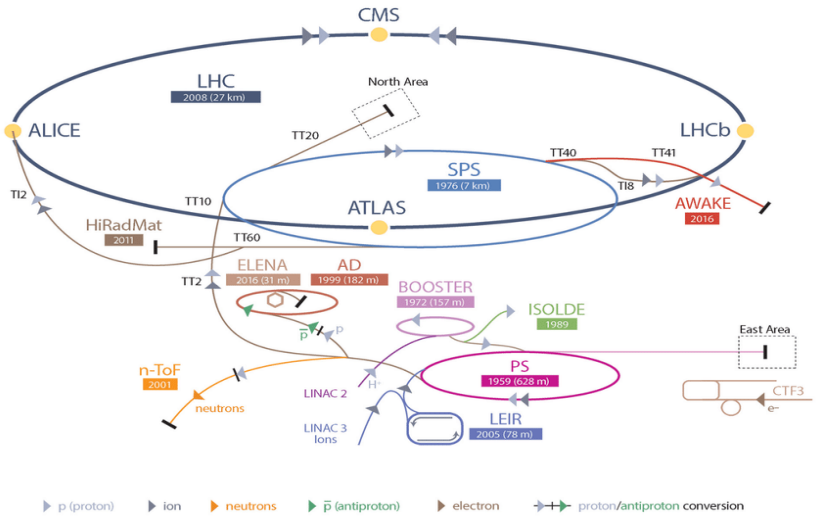


**Figure 2.1:** A Schematic representation of LHC [6].

are held at their circular tracks by 8.33 T magnetic field generated by 1232 superconducting dipole magnets. Almost 392 quadruple magnets focused the beams, with eight radio-frequency (RF) cavities per beam accelerating the particles and ensuring high luminosity. The luminosity ($\mathcal{L}$) of any particle accelerators which define the number of collision events per second with a given cross section area. After a long shutter-down at the end of 2018, LHC reached its peak luminosity of $2 \times 10^{34}$ cm$^{-2}$s$^{-1}$. The accumulated integrated luminosity from LHC operations until 2018 was 190 $fb^{-1}$. At the conclusion of LHC Run 3, projected to occur in 2024, this value is anticipated to increase to 350 $fb^{-1}$. Some fundamental parameters of LHC are given:

### 2.1.1 High-Luminosity LHC Upgrade

The commencement of the High Luminosity (HL-LHC) era is scheduled after the conclusion of the LHC's third extended maintenance period, known as LS3, occurs between 2025 and 2027, when the accelerator is upgraded to reach an instantaneous luminosity of $5 \times 10^{34}$ cm$^{-2}$s$^{-1}$ and up to $7.5 \times 10^{34}$ cm$^{-2}$s$^{-1}$. With HL-LHC's combined luminosity, we will be able to study the Higgs boson, rare decay and search for physics beyond the standard model easily. Figure 2.2 shows plan for this upgrade. The real parameters for the LHC are in table 2.1.

### 2.1.2 CMS Detector Design

As part of CMS detector, two endcap disks are attached to the beam pipe, giving it a cylindrical barrel shape with a length of 21 meters, diameter of 7.3 m, and weight of 14,000 tons. This


**Figure 2.2:** LHC project schedule including the plan for forthcoming high luminosity enhancement [7].

| Parameters | Values |
|---|---|
| Circumference | 27 km |
| Beam energy in collision | 7 TeV |
| Beam energy at injection | 0.45 TeV |
| Bending Field | 8 T |
| Luminosity | $10^{34} cm^{-2} s{-}1$ |
| Beam intensity | 0.56 A |
| Radiated power per beam | 3.8 KW |
| working temperature | 1.9 K |

**Table 2.1:** This Table lists the essential LHC real parameters

sensor is situated within an underground chamber that reaches a depth of 100 meters beneath the region of Cassy, located in France.

**Compact:** Due to the detector's small dimensions compared to its mass.

**Muon:** Due to the muon system in the detector's outer layer.

**Solenoid:** In CMS, there are different layers, each layer consists of a subdetector designed for stopping, tracking or measuring particles emerging from proton-proton or heavy-ion collisions. There are four major sub-detectors in it, as shown in Figure 2.3. There are three sub-detectors inside a superconducting solenoid magnet: the particle tracking system, the calorimeter, and the system to measure the energy generated by electromagnetic and hadronic interactions. An iron magnetic flux return yoke surround the solenoid magnet and consists of a mu-meson subdetector. These sub-detectors with different materials are used to give information about

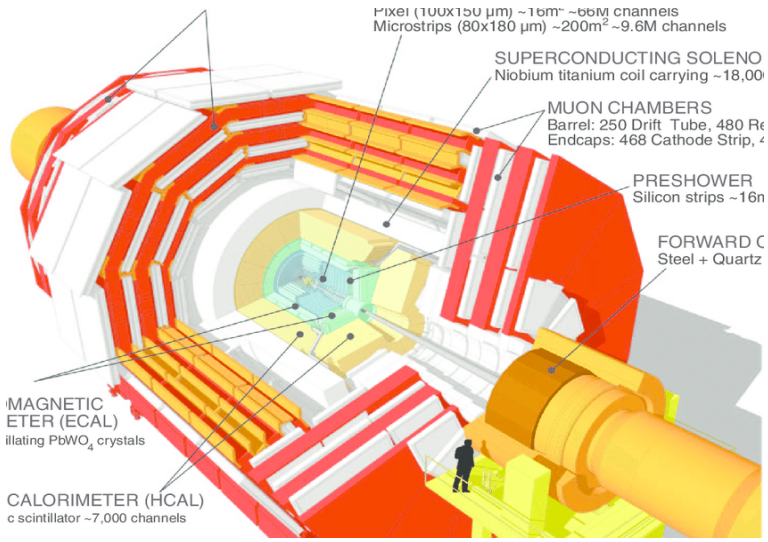


**Figure 2.3:** A perspective view of the CMS detector [8].

different particles and measure their energy, momentum and charge and hence identify them. As a result of the solenoid magnet's high magnetic field (3.8 T), all charged particles that are impacted by the collision have enough bending power to bend.

In tracking detectors, the precision measurement of particle track curvatures is used to identify particle charge and momentum. By using the electromagnetic calorimeter, photons and electrons produce electromagnetic showers, and with these showers, particle energy is measured. The more penetrating hadrons such as charged pions produce hadronic showers in the hadronic calorimeter, which help in measuring their energy. Muons are the only particles that can traverse all the subdetectors and reach the muon system [32].

Figure 2.4 shows that when different types of particles pass through the CMS sub-detector and then by Combining the information from different subdetectors helps in discrimination between particles. As we can see from the figure both photons and electrons leave showers in the electromagnetic calorimeters but photons don't leave tracks in the tracking system and hence we can distinguish photons and electrons. With the help of these we can also identify charged and neutral hadrons.

### 2.1.3 The Coordinate System used by CMS

In describing the compact muon solenoid structure, the standard coordinate system is defined, with the interaction point at the center of the LHC ring and the y-axis is perpendicular to the x-z plane and points vertically upward as shown in figure 2.5. An azimuthal angle called

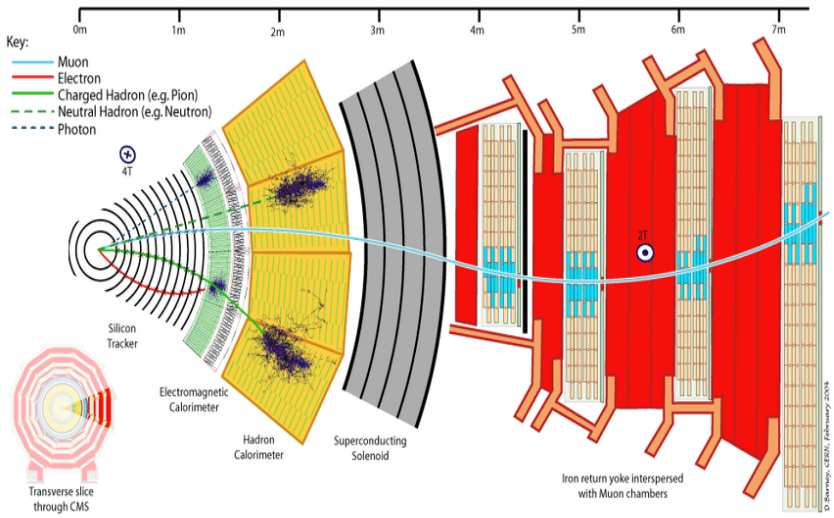


**Figure 2.4:** Cross-sectional View of the CMS Detector Showing Signatures of Detected Objectives [9].

$\phi$ is defined in the x-y plane with $\Phi = 0$ for the x-axis of the LHC ring and $[-\pi, +\pi]$ for the other two values. The polar angle is defined such that $\theta = 0$ lies along the beam pipe in the positive-z axis and takes values of $[0, +\pi]$. Due to the fact that particles resulting from proton collisions have significant boosts along the collision axis and are randomly distributed in the angle $\theta$. Pseudorapidity $\eta$ is an alternative kinematic variable which is more advantageous. This pertains to the distribution of particles' angles, not their energy. The calculation of $\eta$ is done utilizing the following formula 2.1.1:

$$\eta = tan(\theta/2) \tag{2.1.1}$$

The small (larger) values of $\eta$ indicate that particles lie at a right angle to the beam axis. According to the formula 2.1.2, the distance between particles is expressed as the two-dimensional angular distance ($\Delta R$) in the $\eta - \phi$ plane:

$$\Delta R = \sqrt{\Delta\eta^2 + \Delta\phi^2} \tag{2.1.2}$$

A second useful variable is $P_T$, which is expected to be negligible before the collision. Parton momentum should be longitudinal (along the beam axis) before the collision. As a result of the conservation of momentum, it is possible to quantify an imbalance in the outgoing particle's energies using transverse momentum. As a result, the Dark Matter candidate used in this analysis is outgoing particles that escape the detector without leaving a signature.

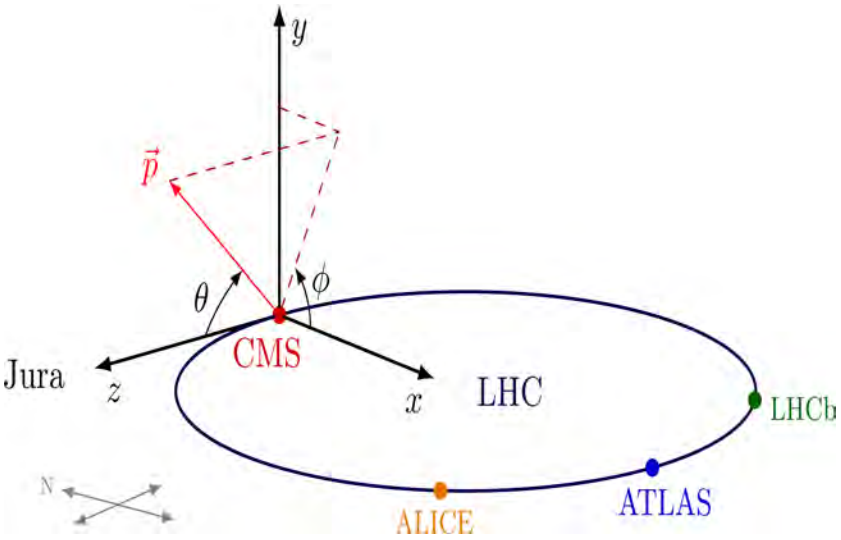


**Figure 2.5:** The CMS Coordinate System [10].

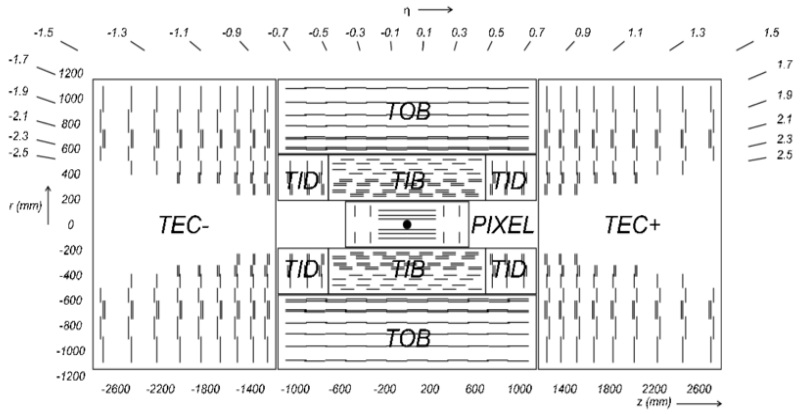


**Figure 2.6:** CMS Tracker System [10].

## 2.2 CMS Tracking System

Tracker silicon (first subdetector) located near the interaction point, requiring radiation resistance of the material. The diameter and length are 2.5m and 5.8m respectively, covering a Pseudorapidity range of $|\eta| < 2.5$. A tracking system allows for high-resolution measurement of charge and momentum as charged particles propagate away from the collision point. All charged particles can be reconstructed from the collision point by the tracker, allowing very high resolution-identification of primary and secondary vertices. At the inner radius of the tracker is a silicon pixel subdetector, and at the outer radius is a silicon strip subdetector. Figure 2.6 provides an overview of the CMS tracker system and its four subsystems, Pixels, Outer Barrels (TOB), Inner Barrels (TIB), and End Caps (TEC).

**Figure 2.7:** Schematic view of Silicon Pixel detector [11].

Tracker consists of two parts:

### 2.2.1 Silicon Pixel Detector

Pixel tracker has the ability of correctly reconstructing both primary proton proton interaction vertices and secondary vertices associated with decay of large particles including b-hadrons. There are 2-endcaps and a barrel region in the silicon pixel detector. Pixel detectors have three-barrel layers with a radius of 4.4 cm, 7.3 cm, and 11 cm. There are approximately 66 million channels in a silicon pixel detector. A schematic diagram of the Silicon pixel detector can be seen in figure 2.7.

1184-pixel sensor modules are mounted in the pixel detector's barrel region. Approximately radial distance ranging from 300 mm to 160 mm from point of collision and 548.8 mm is the length from which the collision is located. An individual module contains a sensor with a resolution of 6650-pixels and a measurement area of 100 $\mu$m $\times$ 150 $\mu$m.

### 2.2.2 Silicon Strip Detector

In addition to the inner pixel detector, silicon strip detectors also contain 10 million channels. They have a barrel region and endcaps similar to pixels. The tracker silicon strip is comprised of ten layers in the barrel region and nine layers in each detector endcap. As shown in figure 2.8, it is comprised of four components. The Silicon Strip detector is the largest silicon tracker ever produced. The tracker's inner barrel consists of four cylindrical layers arranged along the

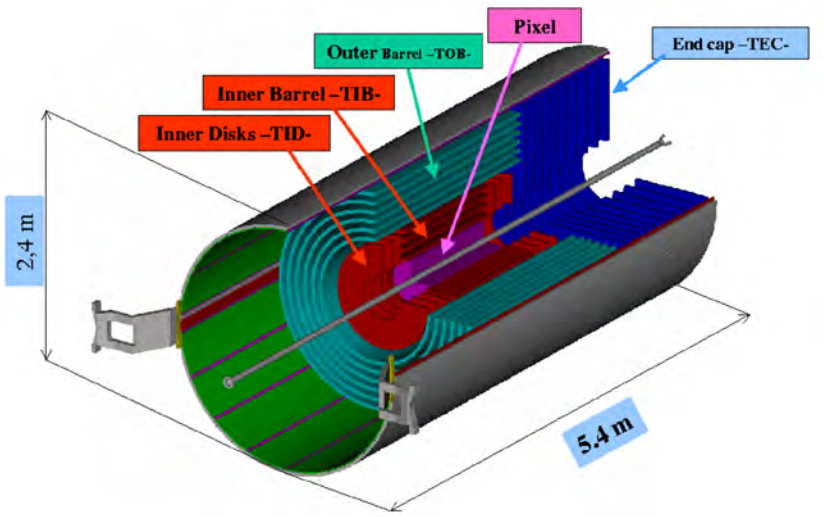


**Figure 2.8:** Mechanical layout of the pixel and strip tracker [11].

"Z" axis, spanning from -700 mm to +700 mm. These layers have radial distances of 255 mm, 339 mm, 418.5 mm, and 498 mm.

## 2.3 Sub-detectors for Calorimetry Measurements

Placed beside the tracking system and within the solenoid magnet, the calorimeter sub-detector measures neutral and charged particles. By measuring the energy lost by incident particles due to collisions with the detector material, it is able to identify the incident particle based on the depth at which it penetrates into the calorimeter. It is impossible to detect neutrinos with such a calorimeter and they escape the detector, but they can be inferred by the apparent energy imbalance in the collision. Among the three calorimetry subdetectors in the CMS detector are:
**Electromagnetic calorimeter (ECAL)**: A detector that measures electrons and photon energies is referred to as an electromagnetic calorimeter.
**The hadronic calorimeter (HCAL)**: It measures hadronic energy.
**Forward calorimeter (FCAL)**: The third detector is called a forward calorimeter which measure the particle energies in the detector's very forward regions.

### 2.3.1 Electromagnetic Calorimeter

Electromagnetic Calorimeters (ECAL) are used to measure energy very precisely. ECAL is the only subdetector that provides information about photons, which is essential for analyzing the

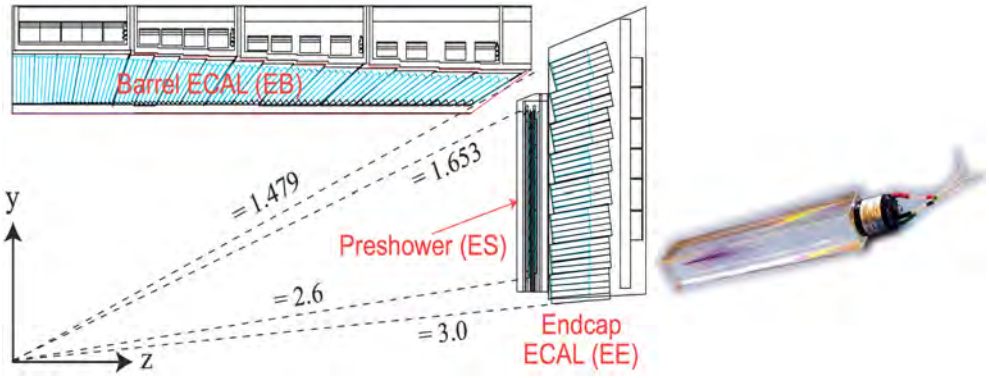


**Figure 2.9:** Image of a longitudinal section of the CMS electromagnetic calorimeter showing the barrel of the ECAL and an endcap of the ECAL [12].

Higgs boson decay. Electron reconstruction is also possible using the ECAL, which combines its information with a tracker to obtain very precise measurements of electron position and energy to analyze the multi-lepton final state. In the calorimeter, when these particles interact with the material, electromagnetic showers are formed. Consequently, the particles in the calorimeter have come to rest. In ECAL, Lead Tungstate ($PbWO_4$) crystals serve as scintillators (which emit light when in contact with particles) that are read by an avalanche photodiode that has an output proportional to the amount of energy deposited.
The ECAL provides a Pseudorapidity coverage of $|\eta| < 1.479$ in the barrel which is called the ECAL Barrel (EB), and ECAL Endap (EE). Figure 2.9 shows the ECAL barrel and an ECAL endcap.

Preshower (ES) detectors are installed in front of the ECAL endcaps in the forward region of the detector for detecting single photons as well as photons resulting from the decay of the pion into two photons $\pi^0 \rightarrow \gamma\gamma$ very close to each other. Figure 2.10 shows the longitudinal image of the CMS calorimeter portion, which shows the ECAL barrel and endcap.

### 2.3.2 Hadronic Calorimeter

There are three parts of the hadronic calorimeter (HCAL) that work together to measure the energy and location of hadronic jets. Figure 2.11 illustrates how the HCAL works:

**the HCAL Barrel detector (HB)**
**the HCAL End-cap detector (HE)**
**the HCAL Forward detector (HF)**

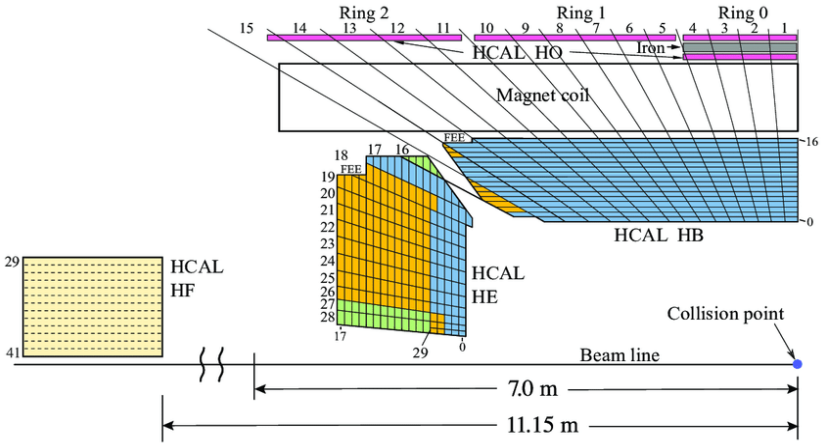


**Figure 2.10:** Using its four primary components, the CMS HCAL (Compact Muon Solenoid Hadron Calorimeter) is viewed using its four primary components: the hadron barrel (HB), the hadron endcap (HE), the hadron outer (HO), and the hadron forward (HF) [13].

In HCAL, thick brass is used as the absorber and plastic fluorescent scintillator is used as the active component. The interaction between the particle and the absorber plate produces secondary particles. These secondary particles may interact as they pass through more absorber layers, creating a "shower" of particles as they pass through more absorber layers. The light emitted by these particles is caused by their movement between alternating layers of active scintillation material. For calculating the particle's energy, the scintillator's total light energy across the particle route is calculated.

## 2.4 Solenoid Magnet and iron Yoke

The solenoid magnet generates magnetic field comes from the superconductivity of the magnet. The superconductivity of the magnet causes the particle paths to bend. Particles with more bent paths have less momentum. The magnet's iron return yoke alone contributes 12500 tones to the whole detector weight of 14000 tones. Iron return yokes are used for the structure building of CMS and as magnetic field absorbers.

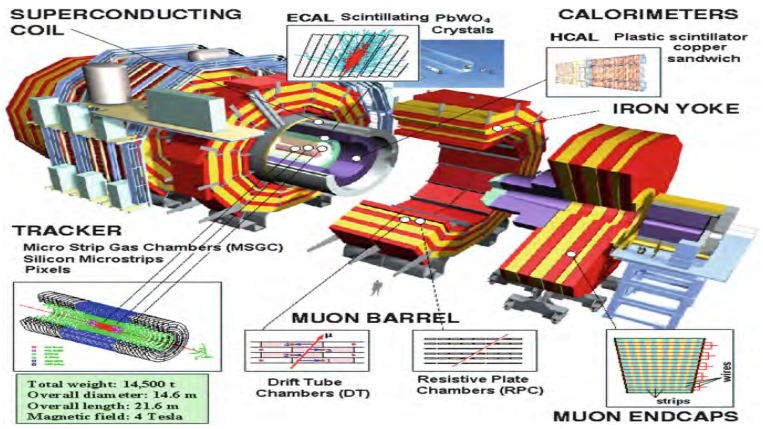


**Figure 2.11:** Illustration of various Sub-detectors of CMS Experiment [14].

## 2.5 Muon System

In CMS muon chambers, gaseous detectors such as drift tubes, resistive plate chambers, and cathode strip chambers are used. CMS muon chambers are built into the iron return yoke of the magnet. Muon position and momentum are measured using these devices. CMS detectors are insulated from all particles except neutrinos by the muon system, which plays a major role in detecting neutrinos indirectly via $E_T^{\text{miss}}$.

## 2.6 Trigger Concept

There are two trigger stages in CMS that lower data production and select events with a high degree of physical interest for storage. Levels $L_1$ are hardware triggers that reduce data from 40 MHz to 100 kHz. Levels $L_2$ are software triggers that further reduce data to 1 Hz.

## 2.7 CMS Phase-2 Upgrade

It is necessary to prepare the complete CMS detector for the requirements of the HL-LHC environment between 2025 and 2027, when the CMS Phase-2 Upgrade will be carried out as shown in figure 2.12. In addition to being able to withstand high amounts of radiation, the new detector must also have a greater degree of energy resolution (granularity) to handle a 140-piece pileup, have greater bandwidth, and provide better trigger performance. The muon system will improve the current gas detectors. In the forward region, gas electron multiplier detectors will be installed.

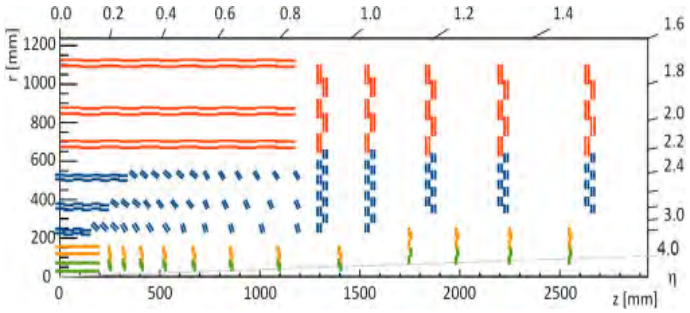


**Figure 2.12:** CMS outer tracker upgrade for HL-LHC [15].

Phase 2 upgrades include replacing the hybrid photodiode readout in ECA and HCAL with silicon photo-multipliers (SiPMs). In 2024, the CMS silicon tracker will be severely damaged by radiation and will require a complete replacement. In 2024, the calorimeter endcaps will also undergo extensive upgrades. Similarly, at above $500\,\mathrm{fb}^{-1}$, the existing forward calorimeter will not perform effectively and will be replaced with the High Granularity Calorimeter (HGCAL).

### 2.7.1 Tracker upgrade

Among the features of the new CMS tracker are a new module design that allows the outer tracker to contribute to the $L_1$ trigger, a decreased materials budget, and longer forward coverage.

A sub-detector is included in the inner tracker, which has the **small pixel detectors**, while the outer tracker contains the **silicon macro pixel detectors** and the **strip detectors**.

#### Tracker Layout and Sensor Module

Designed to ensure robust tracking (reconstruction of particle trajectories) while retaining a low material budget, the updated tracker's layout allows it to provide expanded forward coverage. The Inner Tracker has four-barrel layers and twelve discs on each end, providing forward coverage of up to $\eta = 4$. A total active area of 4.9 $m^2$ is covered by the pixel modules. Outer Tracker is made up of 6-barrel layers and five discs on each end.

The outer tracker consists of a silicon macro-pixel sensor and a silicon strip sensor. These are referred to as "PS modules" and may be found deep inside the Outer Tracker. In the r-z perspective, the CMS Tracker structure consists of four sections. The outer layer modules are often referred to as "2S modules" due to the presence of two silicon strip sensors. The two types of readout chips used by the Inner Tracker's pixel modules are green and yellow. The Outer

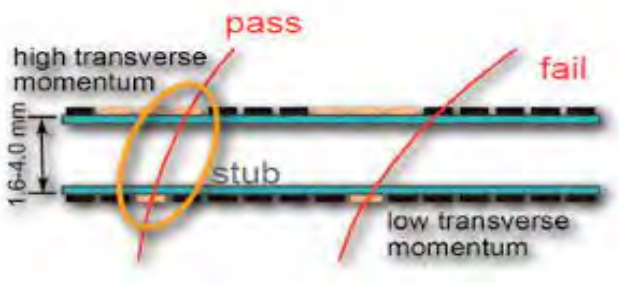


**Figure 2.13:** pT -trigger modules [15].

Tracker has two strip-sensor (2S, red) modules and one strip-sensor and macro pixel-sensor (PS, blue) module shown in figure 2.13.

### 2.7.2 Trigger Input

The Outer Tracker's PS and 2S modules are designed to allow transverse momentum ($P_T$) discrimination at the module level.

Both types of modules comprise two closely stacked, parallel oriented sensors.The special read-out chips correlate the hit positions on both sensors of each module to calculate the particle $P_T$. Stubs are tracks that fall within the search window and have a $P_T$ threshold of 2 GeV. Stubs are sent to the Outer Tracker's back-end electronics at bunch crossing frequency, where they are processed into specific tracking algorithms that reconstruct tracks. The threshold frequency for L1 trigger decision is 750 kHz.

### 2.7.3 High Granularity Calorimeter

Radiation tolerance is exceptional, high-energy showers are accurately measured with the HGCAL, and the L1 trigger decision-making process is enhanced. Silicon sensors and scintillating tiles are used in the calorimeter design. A HGCAL has two compartments: a silicon-based electromagnetic section (CE-E) and a hadronic section (CE-H). These compartments contain silicon as well as plastic scintillators, which are read by SiPMs.

CE-E uses copper, copper-tungsten, and lead plates as an absorbing material which are wrapped in stainless steel. The entire volume calorimeter is thermally insulated and reaches at a constant temperature of 35 °C. Hexagonal P-type sensors are the silicon base material for HGCAL, and they come in two granularity's and three thicknesses (300 $\mu$m, 200 $\mu$m, and 120 $\mu$m) to access for regions of variable fluence inside the detector volume. The maximal fluence val-

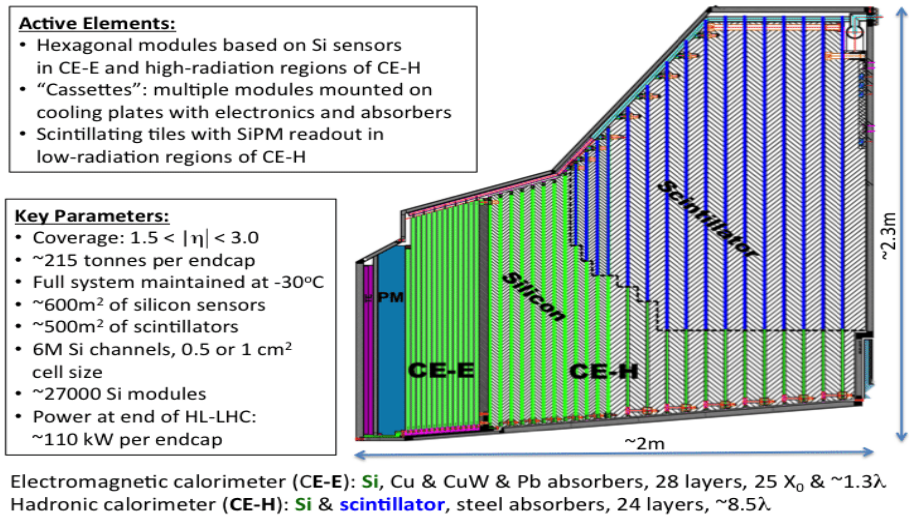


**Figure 2.14:** Cross section of CMS HGCAL [16].

ues for 300 $\mu$m, 200 $\mu$m, and 120 $\mu$m thick sensors are $5 \times 10^{14} n_e\,\mathrm{cm}^{-2}$, $2.5 \times 10^{15} n_e\,\mathrm{cm}^{-2}$, and $7 \times 10^{15} n_e\,\mathrm{cm}^{-2}$ at luminosity of 3000 $\mathrm{fb}^{-1}$. Silicon is used in high density regions of the calorimeter, while scintillators are used in lower-fluence areas. Silicon covers approximately 620 $m^2$. More detail of the HGCAL of the silicon sensor are seen in figure 2.14 above.

Chapter 3

# Dark Matter

## 3.1 Open Questions in SM

Besides having a successful theory, the SM is viewed as being lacking in some key areas. Some of the unanswered questions that SM leaves are as the following.

### 3.1.1 What is the Dark Matter?

The observations of galaxies and stars indicate that there is 95.2% of the universe's mass to be unseen "Dark Matter" [33]. It is necessary to extend the standard model in order to explain dark matter, as the Standard Model does not provide any viable candidates for it. This thesis provides an in-depth examination of dark matter in terms of two Higgs Doublet Model plus Pseudoscalar a (2HDM + a).

### 3.1.2 Gravity

A macroscopic universe is a result of gravity, the weakest of the four fundamental forces. Strong and electroweak forces are explored in the SM, but gravity is not included. Gravity is a force which operates on a much larger scale with a long-range component.

### 3.1.3 Neutrino Mass

Massless neutrinos exist in the SM, but experiments have shown that neutrinos with specific flavors can be measured with a different flavor. If neutrinos were massless, this neutrino oscillation phenomenon would not be possible [34].

### 3.1.4 Matter Antimatter Asymmetry

Why there is no antimatter in the universe? We first need to understand the early stages of universe, either more matter was created or an equivalent amount of matter and antimatter were created, but somehow antimatter vanished. The dominance of matter over antimatter cannot be explained by SM.

### 3.1.5 Three Generation of Matter

With three generations of quarks and leptons and multiple orders of magnitude of difference in fermion masses, the Standard Model fails to fully explain these phenomena.

## 3.2 Evidence of Dark Matter

According to cosmology, the universe's total mass-energy consists of around 4.8% conventional matter, 25.8% dark matter, and 69.4% dark energy. As a result, the majority of our universe remains unobserved. Even though dark matter has not been directly detected, numerous cosmic observations support its existence and give us a better understanding of it. While dark matter's nature remains a mystery, these observations offer valuable constraints.

### 3.2.1 Galaxy Rotation of Curve

Fritz Zwicky discovered the existence of DM in 1933 when calculated the mass of the Coma Cluster (cluster of galaxies) by converting kinetic energy to potential energy using the virial theorem [35]. According to him, the calculated galaxy mass is two hundred times larger than what is expected from visible matter, suggesting that there is non-luminous matter present in the galaxy. It was only after studying galaxy rotational curves that scientists accepted dark matter. A galaxy rotational curve explains how stars and gas move based on their radial distance from its center. Newtonian dynamics predicts that visible matter v(r) decreases as 1/ r, as described mathematically in equation 3.2.1,

$$v(r) = \sqrt{GM(r)/r} \tag{3.2.1}$$

while moving from the center of the galaxy where most of the radiant matter is located as shown in 3.1. The relationship between Newton's constant G and the mass M(r) of observable matter

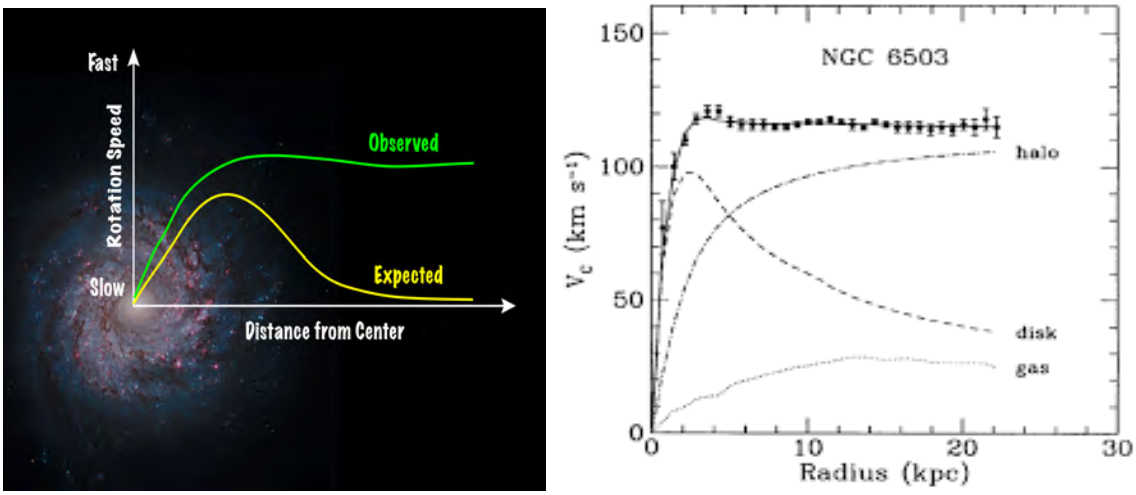


**Figure 3.1:** Rotation curve of NGC galaxy [17].

at a given radius r corresponds to Newton's law of gravitation. However, Ford and Rubin found that as one moves away from galaxy center, the rotational velocity becomes constant. As a result of this observation, the galaxy probably contains a non-radiant dark matter halo. Based on the rotational curve shown in figure 3.1, the rotational velocity of the NGC 6503 galaxy is shown to be different from the expected rotation velocity presuming the spherical nature of a dark matter halo and there is no coupling between dark matter and visible matter. The galaxy center is primarily composed of visible matter, while the dark matter halo dominates at large radii, based on data and predictions.

### 3.2.2 Gravitational Lensing

A simple definition of gravitational lensing is "mass bends light". When light from a distant object passes close to a big object (and hence through its gravitational field), the light will bend, causing the picture of the object to be twisted. Massive objects with strong gravitational fields include galaxies and clusters of galaxies. The deflected light will refocus somewhere else producing single or multiple images of the light source, arcs, or even Einstein rings [36]. Based on equation 3.2.2, we determine gravitational lensing by measuring how much light bends with the mass of the object. Heavy objects bend the light more, leading to more distortion of the image.

$$\alpha = \frac{4GM}{c^2 b} \tag{3.2.2}$$

The image in Figure 3.2 illustrates a X-ray and lensed image of galaxy cluster 1E 0657-56 which can be used to estimate the mass of the object. During collision, the gas particles "normal"

**Figure 3.2:** X-ray observation of the Bullet cluster obtained by Chandra X-ray Observatory. In the red region are the X-ray measurements of hot gas, while in the blue area are the gravitational lensing images of mass distribution [18].

matter" will interact electromagnetically with each other then slow down. Contrary to ordinary matter, dark matter primarily interacts through gravity and does not undergo electromagnetic interactions. Therefore, the majority of the light we observe comes from sources that emit electromagnetic radiation, such as hot objects. The pink region in the image shows X-ray emitting gas, while the blue region indicates dark matter located indirectly through gravitational lensing within the cluster. The observations show that most of the visible matter is now in the centre of the image, but the lensing tells us that most of the mass lies further out which indicate the presence of dark matter.

## 3.3 Using the Dark Matter Puzzle to understand the mysteries of weakly interacting massive particles

As previously discussed, it is worth noting that there is strong experimental evidence in favor of DM. However, these experiments are unable to resolve the question of which particles make up the particle nature of luminous matter. Among the captivating imaginary particle categories that have gained considerable attention WIMPs, denoted by $\chi$. Figure 3.3 explains this phenomenon. It is not accurately defined what would constitute a WIMP, but observation sets certain constraints. The particles were generally defined as being beyond the Standard Model and having masses between 1 GeV and 5 GeV, and gravitational interaction could be weak or only involve an interaction. In order to explain the formation of structures and clumping of

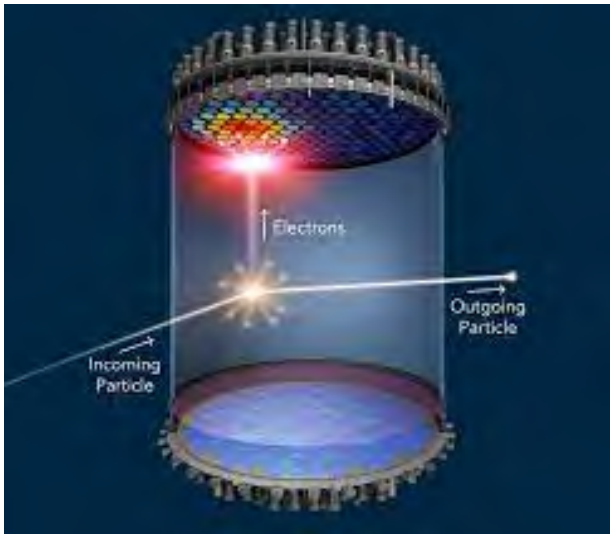


**Figure 3.3:** WIMPs and Dark matter [19].

matter, a WIMP must have a lifetime comparable to our universe's age. A particle exhibiting these characteristics can only be observed to produce dark matter abundance. To explain the formation of structures, the particle must be non-relativistic, which is known as "cold" or clumping of matter. In an early Universe with a high temperature, WIMP pairs would have formed and been annihilated if the WIMPs were in thermal equilibrium with particles from the Standard Model.

$$\chi\chi \longleftrightarrow SM$$

## 3.4 Mono-X Collider Searches

DM particles can be created in a laboratory setting and examined to see if they interact with particles from the Standard Model. The diagram in Figure 3.4 illustrates three methods of DM detection. The interaction is not exact, but depends on which model is being used. On the left-to-right interpretation, the DM would annihilate into particles from the Standard Model. One can suppose that this process occurs in regions of the universe where DM is most dense. This type of search is mostly performed by astrophysical experiments, and it is called an "Indirect search". If we were to flip the diagram and consider the vertical axis as the time axis, we would observe scattering. However, it is important to note that dark matter (DM) does not scatter SM particles in a manner similar to neutrinos interacting with atomic nuclei. This particular search approach is commonly referred to as "direct search". Both direct and indirect searches

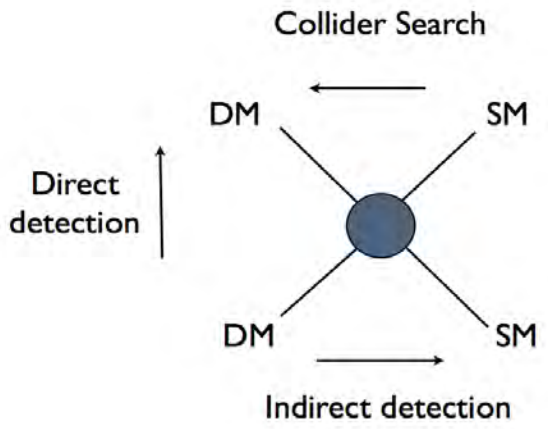


**Figure 3.4:** Diagram showing potential interaction between invisible and particle physics standard model sector.

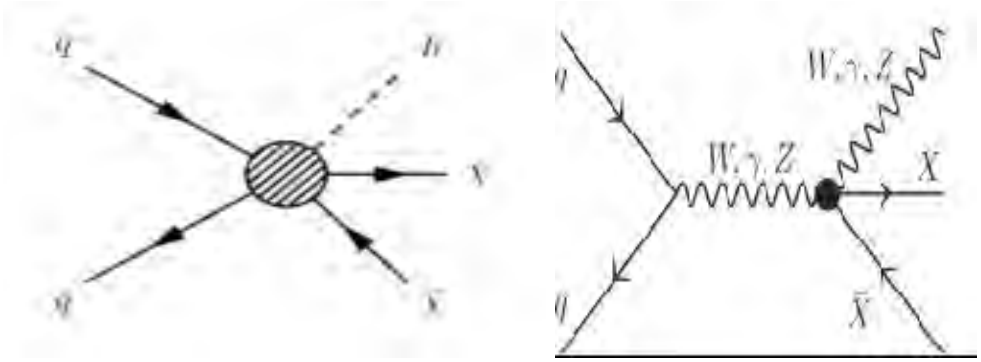

**Figure 3.5:** The depicted Feynman diagrams illustrate the production of dark matter in conjunction with an initial-state radiation (ISR) gluon, photon, Z boson, W boson, or Higgs boson [20].

for dark matter suffer from astrophysical uncertainties due to their reliance on cosmic data. Collider searches, on the other hand, provide a controlled environment to study dark matter in particle colliders, offering higher sensitivity to low dark matter masses. It is possible to detect invisible matter along with standard model particles through the imbalance of total $P_T$, which is called $E_T^{\text{miss}}$. At the Large Hadron Collider (LHC), initial state radiation (ISR) uses particles such as hard gluons and photons to produce heavy Higgs bosons or massive gauge bosons as shown in figure 3.5. As an alternative to effective field theories, simplified models introduce more degrees of freedom and mediating particles.

## 3.5 Beyond the Standard Model (2HDM+a)

I used the two Higgs doublet model (2HDM+a) in this thesis since standard model cannot explain new physics. The type of fermions that couple to the 2HDM doublet determines the type of theory [37]. One of the doublets $\phi_u$ only couples with up quarks, while another doublet $\phi_u$ couples with both up and down quarks in type-II 2HDM.

$$L \subset -y_u Q\bar{\phi}u\bar{u}y_d Q\bar{\phi}d\bar{d} + y1L\phi d\bar{\ell} + h.c \tag{3.5.1}$$

The symbols yu, yd, and yl represent the Yukawa couplings in the Higgs doublet. After breaking symmetry, the new doublets achieve VEVs $v_u$ and $\nu_u$ that can be parameterized as follows:
The neutral CP-even scalars with masses $m_h$ and $m_H$, denoted as h and H respectively, $H^{\pm}$ is the heavy charged scalar with mass $m_{H^+}$ with its antiparticle $H^-$ having mass $m_{H^-}$ and $A^0$ with neutral CP odd having mass $m_{A^0}$.

$$\Phi_d = \frac{1}{\sqrt{2}} \begin{pmatrix} -\sin(\beta)H^+ \\ \nu_d - \sin(\alpha)h + \cos(\alpha)H - i\sin(\beta)A^0 \end{pmatrix}$$
$$\Phi_u = \frac{1}{\sqrt{2}} \begin{pmatrix} \cos(\beta)H^+ \\ \nu_u + \cos(\alpha)h + \sin(\alpha)H + i\cos(\beta)A^0 \end{pmatrix}$$

In the context of the two CP even Higgs bosons, the angle $\beta$ represents the ratio of vacuum expectation values $\tan\beta = \frac{\nu_u}{\nu_d}$ and $\alpha$ is the mixing angle between the CP even scalars h and H. The scalar h is SM Higgs boson with mass $m_h$= 125 $\frac{\text{GeV}}{C^2}$. In the 2HDM with pseudoscalar mediator "2HDM+a" the interaction between the SM and DM particles ocuurs by the CP-odd spin-0 mediator. This is done by mixing pseudoscalar P with CP-odd scalar from Higgs doublet [38]:

$$\mathcal{L} \supset P(ib_p\phi^\dagger u\phi d + \text{h.c.}) + P^2(\lambda_{p1}\phi^\dagger u\phi u + \lambda_{p2}\phi^\dagger d\phi d) \tag{3.5.2}$$

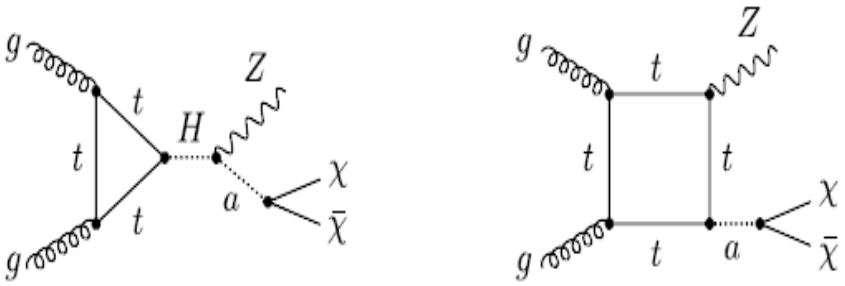


**Figure 3.6:** Feynman Diagram for Z+$E_T^{miss}$ signal [21].

The trilinear and quartic portal couplings, namely $b_p$, $\lambda_{p1}$, and $\lambda_{p2}$, hold significance in the context described. The heavy pseudoscalar $A^o$ interacts with the SM and dark sector, whereas the small pseudoscalar a interacts directly with DM particles. The following parameters have been scanned:

- A measure of the vacuum expectation value for the light and heavy scalars h and H is $\tan\theta$.
- Angle $\sin\theta$ associated with the mixture of Pseudoscalars a and A.
- The Dark Matter mass $m\chi$.

we used the followig benchmark parameters in this research:

$$M_a = 200\,\text{GeV}, \quad M_A = M_H = M_{H^\pm}, \quad m_\chi = 10\,\text{GeV}$$
$$\cos(\beta-\alpha) = 0, \quad \tan\beta = 1, \quad \sin\theta = 3.5\times10^{-1}$$
$$y_x = 1, \quad \lambda_1 = \lambda_{P_1} = \lambda_{P_2} = 3 \tag{3.5.3}$$

Then 'a' decays into a DM pair $a \to \chi\tilde{\chi}$ produced the single-X (referred to as mono-X). There exist multiple channels associated with single-X phenomena that allow studying DM pair production, but we have studied only Z+$E_T^{miss}$. The Feynman diagrams for the above mono-X channels are seen in Figure 3.6. For mono-Z channels, if the $M_H > m_a + m_Z$ (left diagram), as a result, resonant mono-Z production will dominate (right diagram). Description for this model parameters are summarized in Table 3.1.

| **Particle** | **Description** |
|---|---|
| $\chi$ | Fermionic DM Particle |
| $\phi_u$,$\phi_d$ | Two Higgs Doublet |
| h,H | Neutral CP-even scalars, light and heavy |
| a, $A^0$ | CPs of light and heavy mass-even pseudoscalars |
| $H^+_-$ | charge heavy Higgs |
| **Parameters** | **Description** |
| $m_x$ | DM mass = 10 Gev |
| $m_H$ | Mass of heavy neutral CP-even scalar |
| $m_h$ | Mass of light material CP-even scalar, $m_h = 125$ Gev |
| $mH^+_-$ | Mass of heavy charged CP-even scalar |
| $\tan\beta$ | CP-even Higgs boson VEV ratio |
| $\alpha$ | CP-even Higgs boson mixing angle |
| $\theta$ | CP-odd mixing angle between two neutral Higgs bosons |

**Table 3.1:** Parameters description of 2HDM+a

Chapter 4

# Simulation and analysis tools for mono-Z($\ell\ell$)+$E_T^{miss}$ analysis

## 4.1 Event generation at Parton Level

For event generation, we use Madgraph, which is a matrix element generator and a phase-space sampler. We need to provide Madgraph with the 2HDM+a model for our analysis in a Universal FeynRules Output (UFO) format [39]. This UFO file contains the Lagrangian and all relevant Feynman rules having all physical parameters. It generates a matrix element, the corresponding diagrams and the helicity amplitude with ALOHA. With the resulting code, the matrix elements can be evaluated at a given phase space point. The Feynman diagrams for the processes are obtained by considering all possible combinations of external particles and if there are vertices in the UFO allowing the final state particle combinations, the diagram is saved in an output file.

ALOHA creates routines for helicity amplitudes to calculate the matrix element. The advantage of helicity amplitudes is that it is a convenient and effective way to compute the matrix element squared, because it works at the amplitude level, while the trace method, which is based on completeness relations, works on a squared amplitude level. By using helicity amplitudes, the complexity grows only linearly and diagrams can be factorized. This leads to faster computations compared to the tracing technique. All helicity amplitudes from every diagram can be summed and squared to yield the overall result.
In order to calculate the process's total cross section, Monte Carlo integration techniques must be used. Because the integrals cannot be solved analytically, thus solved numerically. To com-

pensate for this, a weight is assigned to each point, corresponding to their contribution to the real distribution. Madgraph then performs an unweighting procedure to turn the weighted samples into unweighted ones. The Parton distribution functions (PDFs) $NNPDF30\_lo\_as\_0130$ and $NNPDF23\_lo\_as\_0130$ are used for mono-Z analysis.

## 4.2 Showering and hadronization with Parton

A simulation chain continues with PYTHIA. It uses the four momenta from incoming particles thus simulate the Parton shower and the hadronization process. The free Partons, including quarks and gluons, out of the initial process, can emit a single gluon. These gluons can again radiate another $qq^{-1}$ pair or a gg pair if they are highly energetic and these quark and gluon pairs still have enough energy, they can radiate yet another quark or gluon pair and so on, as long as they have enough amount of energy. At LHC, we can see the showers induced by the processes as jets. The shower progression within PYTHIA relies on the utilization of DGLAP splitting kernels P(z), describing the probability that a single Parton will split in two with an energy fraction z. These splitting kernels P(z) are derived.

Then hadronization takes place on a low-energetic non-perturbative scale. There the single Partons from the showering process are grouped together in order to form hadrons. The basic principle behind hadronization is the concept of color confinement, so only color-neutral states can exist. In order to simulate hadronization processes, a Lund string framework is used in PYTHIA [40]. Color confinement can be modelled by a color flux tube. In case of colour dipole, the distance between two particles increases, the force between particles grows linearly and the energy decreases. A color flux tube breaks at some point when the energy gets too high and produces a new $qq^{-1}$ pair. At some point only on-shell particles can be produced and the process of hadronization stops. Unstable hadrons decay into stable hadrons, for example pions and other particles decay accordingly to the decay channels implemented in Madgraph or PYTHIA. The output file of PYTHIA contains all the information from showering and hadronization, which includes the mother and daughter particles, the four- momenta of the particles, their status (at which point in the process the particle was created), particle ID and color state. These hadrons and other remaining particles are now passed on to the detector simulation.

## 4.3 Root Analysis Framework

In high energy physics, a framework called ROOT [41] is utilized to evaluate huge amounts of data. It uses the C++ format language. In addition to using histograms and graphing to analyze and visualize the data, curve fitting, functional minimization, statistical tools for data analysis, four vector computation and matrix algebra common mathematical functions, 3D visualizations (geometry), and interface Monte Carlo (MC) events are just a few of the cool packages that ROOT has to offer. A crucial component of ROOT is a data container known as a tree, which contains branches and leaves substructure. ROOT is used for data analysis by a large number of experiments, including BaBar, CDF, PHENIX, and upcoming detectors including ALICE, ATLAS, CMS, and LHCb.

## 4.4 Mono-Z($\ell\ell$) and $E_T^{miss}$ Analysis

This chapter provides detail on the mono-Z + $E_T^{miss}$ analysis, which was performed using $MadGraph5\_aMC@NLO$ (MadGraph5 is a software package which used to generate Feynman diagrams, they are graphical representations of mathematical equations that explain the interactions of particles. The aMC@NLO (Automatic Multi-Channel @ the next-to-leading order) with MadGraph5's extension, higher order corrections can be calculated, which can improve the accuracy of the results) at $\sqrt{s} = 13.6$ TeV. Two Higgs Doublet Model + Pseuduscalar is used for this analysis:

- 2HDM+a (discussed in detail in section 3.5.3) can produce several mono-X signatures. The decay of 'a' results in a mono-X signature caused by the decay of dark matter particles $\chi\chi$. The Z+ model is described here in more detail. It produces a mono-Z signal by decaying heavy neutral Higgs (H) into a Z boson and a pseudo-scalar 'a' as shown in figure 4.1. Two DM particles with missing momentum are analyzed in this signal, as are two boosted Z bosons decaying into two charged leptons, either $e^+e^-$ or $\mu^+\mu^-$. The charge lepton is easier to detect than the jet.

### 4.4.1 Signal Samples

The mono-Z ($\ell\ell$)+ $E_T^{miss}$ signal samples have been studied using MadGraph, Parton Dis- tribution Function (PDFs) NNPDF30_lo_as_0130, PYTHIA 8.3 for Parton showering, and Pseudo-scalar_2HDM UFO model. The gluon gluon fusion is generated using the MadGraph5 syntax. MG5_aMC > import model Pseudo-scalar _2HDM

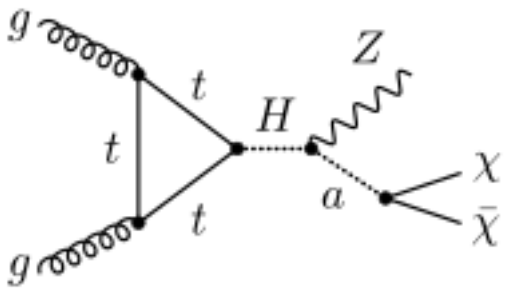


**Figure 4.1:** An illustration of the Feynman Diagram shows the final state of the Z boson decaying to a pair of leptons, followed by the decaying pseudoscaler a [21].

MG5_aMC > generate g g > xd xd  / h1 [noborn=QCD]
Here **xd** and `xd~` are dark matter particles and antiparticles have Particle Data Group IDs are 52 and -52 respectively. The noborn ensures that no tree level contribution will be included and QCD ensures that only color charge particles (quarks and gluons) will participate in the loop.

### 4.4.2 Standard model Background Processes

There are also possible mono-Z($\ell\ell$) signatures that can result from SM processes, in addition to potential DM signals. ZZ, Z+jets, WW, $t\bar{t}$, WZ and W+jets are the supreme backgrounds in this analysis. Based on MC simulation, these backgrounds are compared to the signal's final state.

#### 4.4.2.1 $t\tilde{t}$ Production

Based on figure 4.2, $t\tilde{t}$ production accounts for a majority of background processes caused by leptonic decays. Each top quark decays into a b-quark and a $W^{-1}$ boson, which further decays into charge leptons and neutrinos. Due to the fact that neutrinos are not observed in the detector and do not interact, their presence can only be inferred indirectly from $E_T^{miss}$. As a result, leptonic decay of $t\bar{t}$ can produce a mono- Z($\ell\ell$)signature.

#### 4.4.2.2 Di-Bosons Processes

ZZ and WW di-bosons production are the main backgrounds in the mono-Z channel. In the ZZ process, one Z boson decay to $\ell\ell$ while the other Z boson decay to $\nu\nu$. On the other hand, in

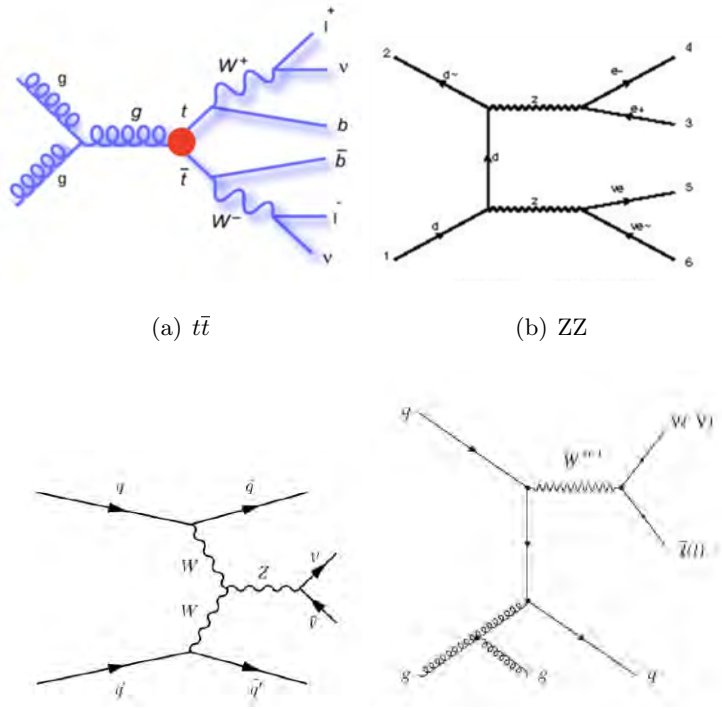


(a) $t\bar{t}$ (b) ZZ

(c) Z+Jets (d) W+Jets

**Figure 4.2:** In Feynman diagrams, $t\bar{t}$ ZZ (top row right), Z+jets (bottom row left), and W+jets (Bottom row right) are shown [21].

the WW process, one W decay to $\ell\nu$ and the other W also decays to $\ell\nu$ as shown in Figure 4.2 (top right). These are simulated at leading order.

#### 4.4.2.3 V+Jets

Figure 4.2 (bottom row) indicates the Feynman diagram for vector bosons (Z, W) production plus, jets. There is sufficient energy left over from the decay of the Z-boson into two neutrinos. Also, W decays to neutrino and charge lepton which also produces some missing energy, but missing energies in V+jets are small compared to the signal.

### 4.4.3 Variation of Parameter

To choose the best value for the analysis, we did scans for $sin\theta$, $tan\beta$ and $m_\chi$.

#### 4.4.3.1 Sin$\theta$

In the $Z + E_T^{miss}$ channel, heavy neutral Higgs (H) decay to a Z-boson and pseudo-scalar a, and the relevant coupling scale is $g_{HZa} \propto sin\theta$, it means that the mono-Z signal will vanish in the limit of $sin\theta \to 0$. In Figure 4.3 left, I plotted the mixing angle between the two neutral CP odd Higgs bosons against the cross-section at different values of $sin\theta$.

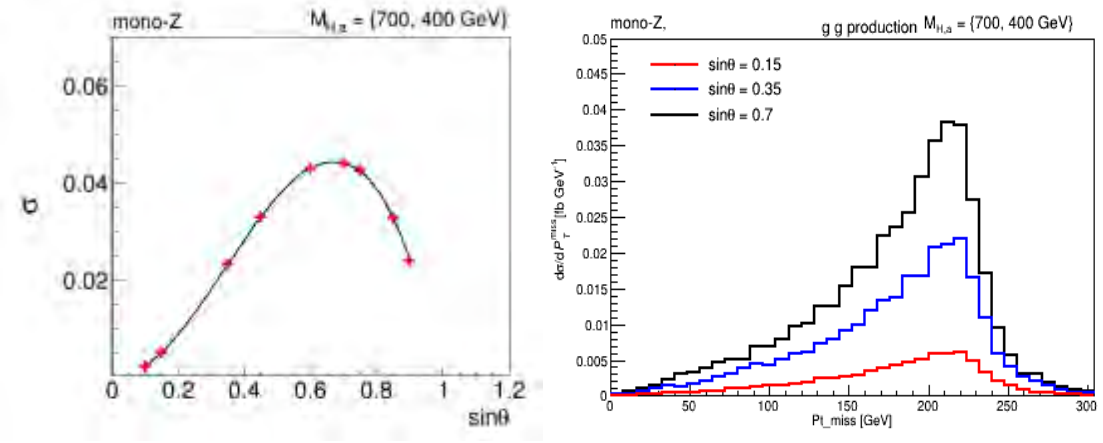


(a) Cross sections against sin$\theta$

(b) mono-Z production for various values of sin$\theta$

**Figure 4.3:** $E_T^{miss}$ distributions for mono-Z production for various values of $sin\theta$. Other parameters are set to 3.5.3 using $M_a = 400$ GeV and $M_A = M_H = MH^{\pm} = 700$ GeV

#### 4.4.3.2 tan$\beta$

A Higgs boson's vacuum expectation value (VEV) is defined as $\tan\beta$, which represents the ratio between two CP-even VEVs. We take different values of $\tan\beta$ and plot them against the cross-section, as shown in Figure 4.5 (left). As the value of $\tan\beta$ increases, the cross-section decreases. Therefore, we have chosen $\tan\beta = 1$ as the benchmark parameter.

The distribution of $E_T^{\text{miss}}$ in mono-Z production for various $\tan\beta$ values is depicted in diagram figure 4.5 (right).For the given parameters $M_a = 200\,\text{GeV}$ and $M_A = M_H = M_H = 700\,\text{GeV}$, these distributions exhibit less sensitivity to changes in $\tan\beta$.

#### 4.4.3.3 m$\chi$

The m$\chi$ is a DM particle mass. By changing the value of m$\chi$ we learn that for which value we can get better signal sensitivity. In Figure 4.4 (left), we can see that the cross-section is almost same for m$\chi \leq 100$, that's why we choose m$\chi$= 10 GeV. The modifications of the $E_T^{miss}$ spectrum in Z + $E_T^{miss}$ production under the variation of m$\chi$ are shown in Fig. 4.4 (right). The

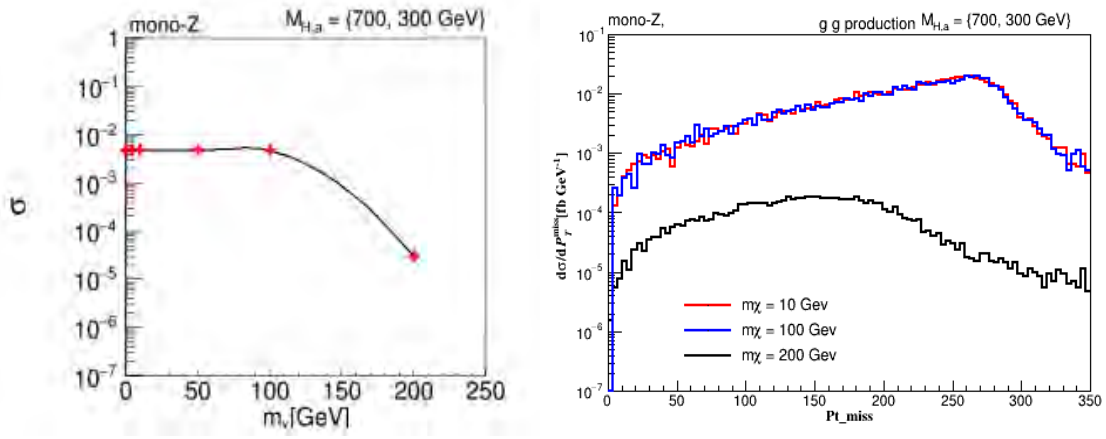


**Figure 4.4:** $E_T^{miss}$ distributions for mono-Z production for various values of $m\chi$. Other parameters are set to 3.5.3 using $M_a = 300$ GeV and $M_A = M_H = MH^{\pm} = 700$ GeV

given distributions correspond to the benchmark parameters in which Ma = 300 GeV , and MA = MH = $MH^{\pm}$ = 700 GeV. The green and blue histograms correspond to the scenario with Ma > 2m$\chi$ lead to almost identical rates of $E_T^{miss}$ spectra, while the red histogram corresponds to the scenario where Ma < 2m$\chi$ which is kinematically not allowed, that's why the cross-section is reduced and the shape is also changed.

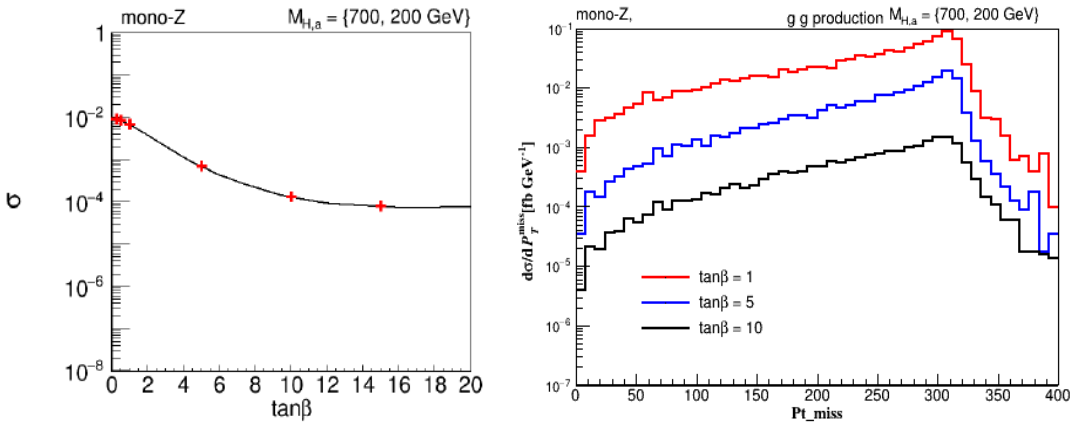


**Figure 4.5:** The distribution shows that for $\tan\beta \leq 1$, we have maximum cross-section (left). $E_T^{miss}$ distributions for mono-Z production (right). The 2HDM + a parameters are set to (3.5.3) using Ma = 200 GeV and $M_A = M_H = MH^{\pm}$= 700 GeV

## 4.5 Optimization of Variables

### 4.5.1 Transverse Momentum (Pt)

The transverse momentum of a particle refers to its momentum that is oriented at a right angle to the direction of the beam axis. The mathematical expression for transverse momentum ($P_T$) can be written as:

$$P_T = \sqrt{P_x^2 + P_y^2}$$

**Missing Transverse Energy** ($E_T^{miss}$): There is a signature left in the detector by all outgoing particles from the collision, except neutrinos which leave without interacting called "hypothetical neutral weakly interacting particles". To ascertain this value, one can examine the momentum disparity within the transverse plane (a plane perpendicular to the beam direction). The distribution of signal for $E_T^{miss}$ is shown in figure 4.6.

Different particles, such as the W boson, top quark, and tau lepton decays, are important in understanding SM physics, but neutrinos are also part of the search for physics beyond the standard model. Among the explorations for elusive dark matter, super-symmetric particles, and extra dimensions, a new particle based on the existence of hypothetical neutral massive particles with weak interactions. In a particle flow (PF) reconstruction, the MET is characterized as the inverted vector summation of the transverse momentum from all reconstructed particles.

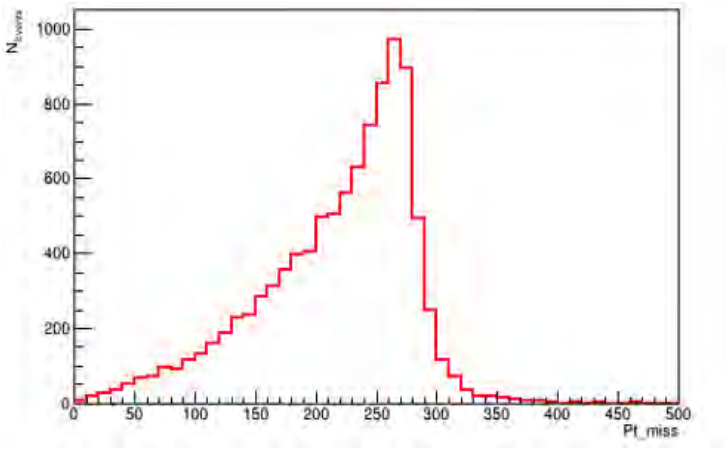


**Figure 4.6:** $P_T^{miss}$ of signal

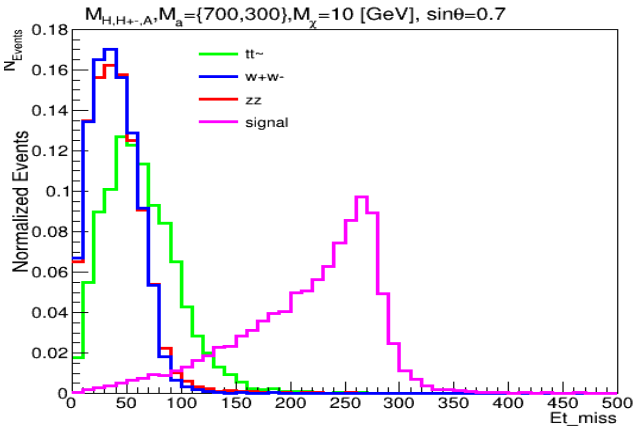


**Figure 4.7:** $E_T^{miss}$ of signal and backgrounds.

### $E_T^{miss}$ of Signal and Background

I generated a plot showing $E_T^{miss}$ distribution of background events relative to a signal. The signal's $E_T^{miss}$ corresponds to a value of $\sin\theta = 0.7$. The remaining parameters are fixed, with $M_a = 400$ GeV and $M_A = M_H = MH^{\pm} = 700$ GeV. Based on our observations from the plot, implementing a $E_T^{miss}$ cut of $\geq 130$ GeV effectively discriminates against the background events. The $E_T^{miss}$ distribution shown in figure 4.7, with a signal significance peak 4.8 around 130 GeV and a range from 0 to 500 GeV.

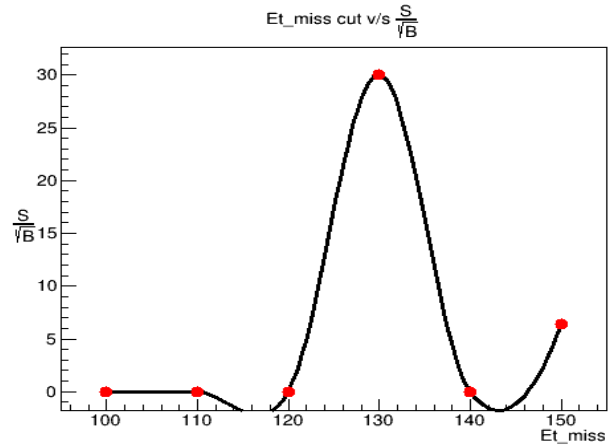


**Figure 4.8:** $E_T^{miss}$ significance.

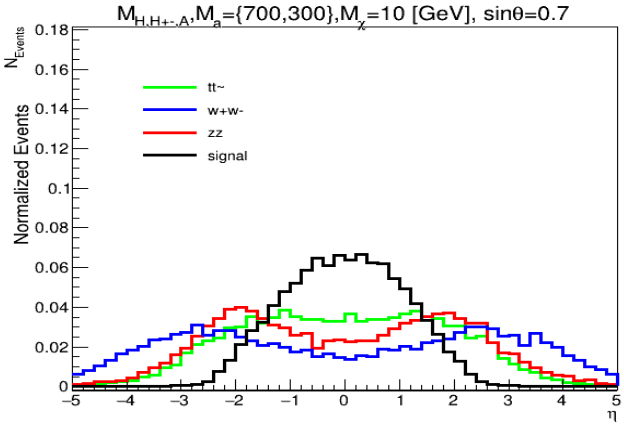


**Figure 4.9:** The signal and background distributions using $\eta$ variable.

### 4.5.2 Pseudorapidity ($\eta$) of signal and background events

It is defined as the angle between the particle's trajectory and the axis of the colliding beams. This characteristic proves valuable in scenarios where accurately measuring the particle's energy is challenging or when the energy is not well-defined. Figure 4.9 illustrates the distribution of $\eta$ for signal events as well as background events. $\eta$ is often used to describe the Pseudorapidity coverage of a detector in particle physics. Significance of signal in $\eta$ is given in figure 4.10, which is maximum at 2.

### 4.5.3 Angle ($\phi$) distribution of both the signal and background events

The azimuthal angle ($\phi$) is defined as the angle between the beam axis and the transverse momentum of a particle or a jet of particles. It provides information about the rotational

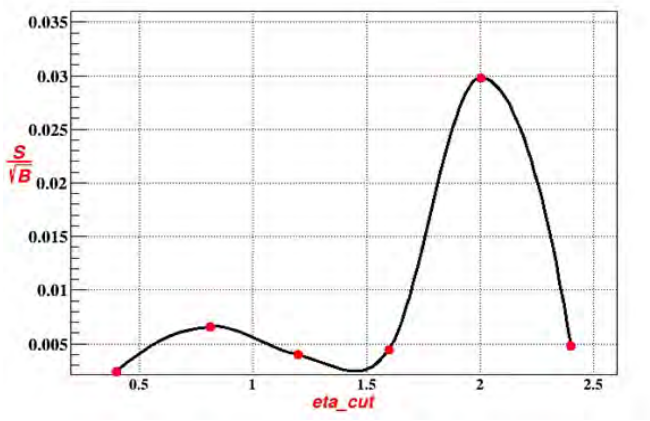


**Figure 4.10:** Significance of signal in $\eta$.

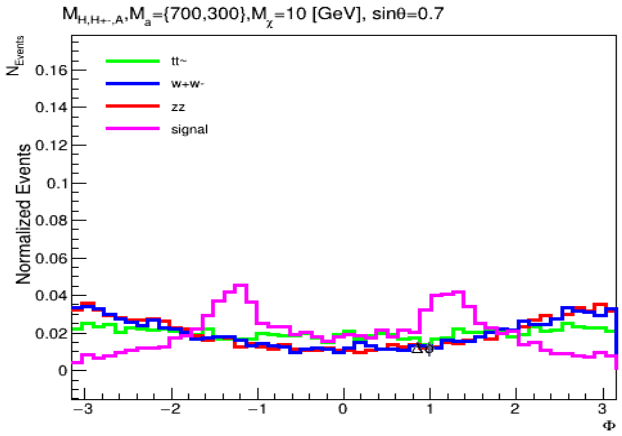


**Figure 4.11:** The distribution of signal and background is characterized by the variable $\phi$.

symmetry around the beam axis. Like $\eta$, $\phi$ also used to describe the detector's coverage in particle physics. Figure 4.11 shows the $\phi$ distributions of the signal and background events.

### 4.5.4 Invariant Mass (M) of signal and backgrounds

Invariant mass in particle physics refers to the mass of a system of particles measured in a way that remains constant for all observers, regardless of their relative motion. In experiments, the invariant mass is used to determine the total mass and energy distribution within a system [42]. I measured the invariant masses of final state leptons having Id's 11, 11 and 13, 13 and plot them in the same canvas. Figure 4.12 shows plot of invariant mass for signal and backgrounds. Here applying cuts for background-signal discrimination is limited, as implementing cuts around 91 leads to signal loss.

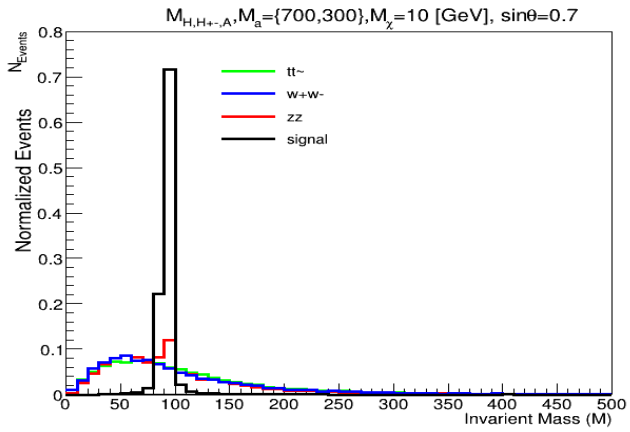


**Figure 4.12:** Invariant mass (M) of signal and backgrounds.

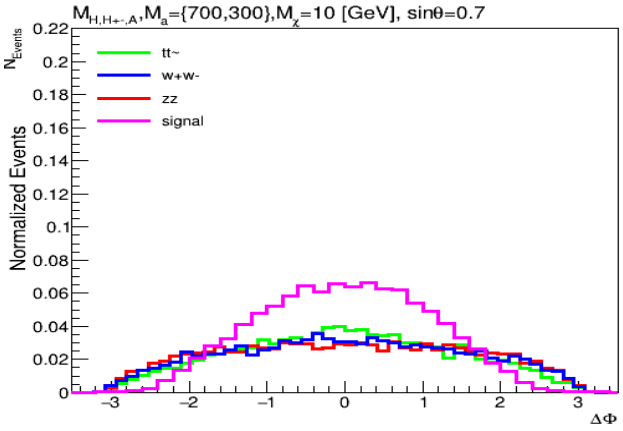


**Figure 4.13:** The distribution of $\Delta\phi$ between final state leptons.

### 4.5.5 Difference in azimuthal angle ($\Delta\phi$) between final state leptons

The difference in azimuthal angle between particles or jets, denoted as $\Delta\phi$, is commonly utilized to analyze correlations among particles generated in high-energy collisions, such as those at the LHC. Figure 4.13 illustrates a correlation between the transverse momentum of leptons e.g($e^-$ $e^+$, $\mu^-$ $\mu^+$). I applied $\Delta\phi$ cuts starting from <= 2.25. So it gives me signal significance peak about 2 4.5.5.

### 4.5.6 Angular separation ($\Delta R$) between leptons

In particle physics, "ΔR" is often used to quantify the angular separation between two particles. It is a measure of the distance in the space of rapidity (y) and azimuthal angle $\phi$ between two

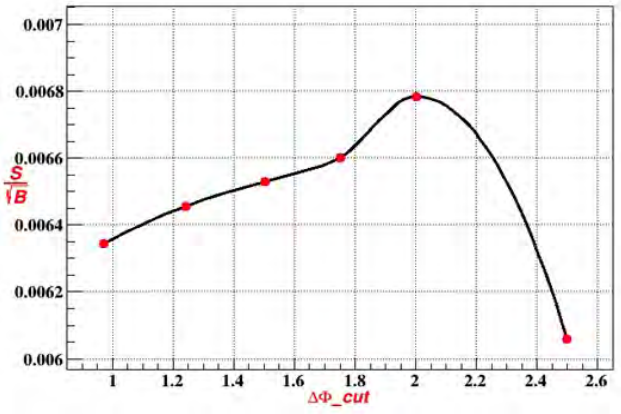


**Figure 4.14:** Signal significance in $\Delta\phi$

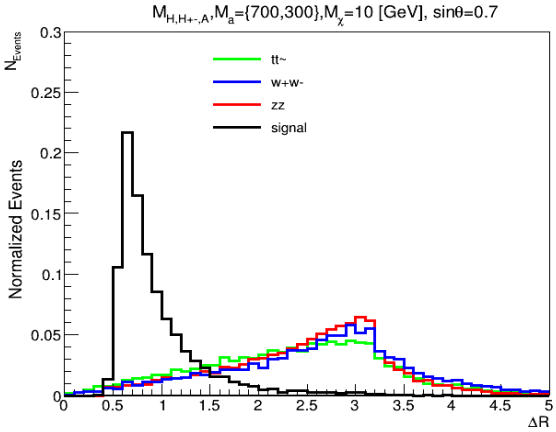


**Figure 4.15:** The distribution of ΔR in Di-leptons final states.

particles. The formula for delta R is::

$$\Delta R = \sqrt{(\Delta\eta)^2 + (\Delta\phi)^2}$$

Here, $\Delta\eta$ represents the difference in rapidity between the two particles, and $\Delta\phi$ represents the difference in azimuthal angle. The rapidity (y) is related to the particle's momentum and mass, while the azimuthal angle $\phi$ represents the angle of the particle's path in the transverse plane. Figure 4.15 shows distribution of ΔR of signal and backgrounds. So here ΔR cuts are possible. I applied cuts starting from <= 1.75. So it gives me signal significance with a peak around 1. Here 4.16 is the significance plot for ΔR.

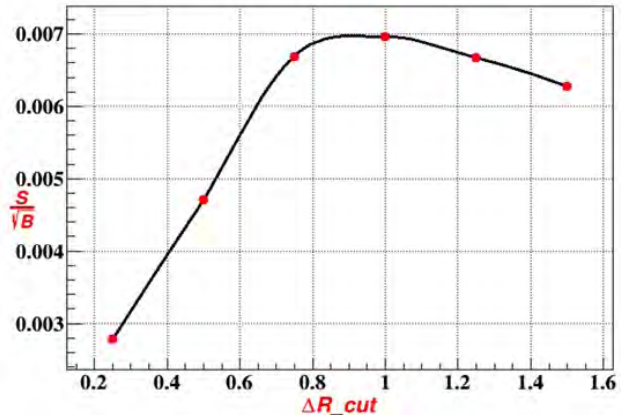


**Figure 4.16:** Significance of signal in $\Delta$R .

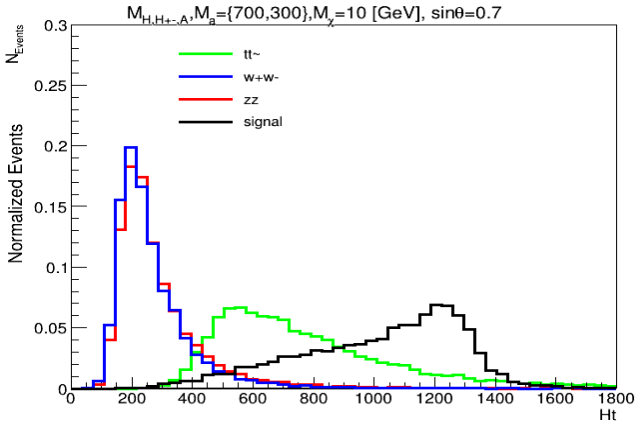


**Figure 4.17:** Scaler sum of transverse momenta in Di-leptons final state.

### 4.5.7 HT

In particle physics, HT signifies the "scalar sum of transverse momenta" or "scalar sum of transverse energy." It plays a key role in studying high-energy collisions as in particle accelerators like the Large Hadron Collider (LHC). *Ht* distribution for signal and backgrounds is given in figure 4.17.

Figure shows that if we apply *Ht* cut at almost 880 then backgrounds should be discriminating from the signal. Figure 4.18 shows significance of signal after *Ht* cuts applied.

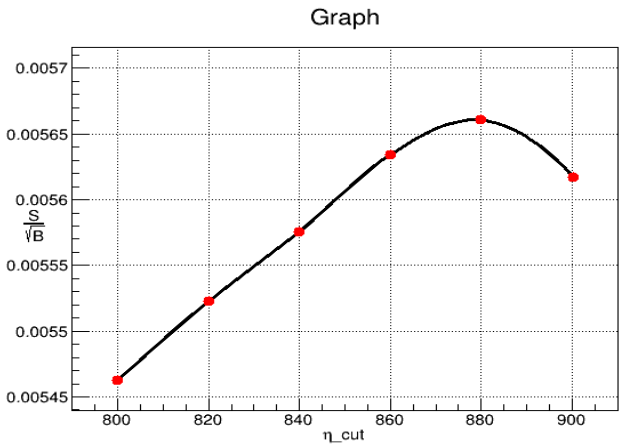


**Figure 4.18:** Signal significance in *Ht*.

## 4.6 Signal Significance

The experimentalists employed the formula $\frac{S}{\sqrt{B}}$ to assess the significance of a signal in relation to the background. In this formula, "S" represents the number of signal events, and "B" represents the number of background events. So, this is actually the final significance which shows the strength of signal. The variables where signal and backgrounds are best discriminated includes $E_T^{miss}$, $\eta$, $\Delta$R, $\Delta\phi$ and HT. So final significance will obtained when we applied cuts on given variables at the same time. My summery table is presented at the end as conclusion chapter, Events after applying final cut on all the variables at the same time;

$$t\tilde{t} = 3888000; \quad ZZ = 2229.497; \quad WW = 505.197; \quad \text{Signal} = 941.04 \tag{4.6.1}$$

$$\frac{S}{\sqrt{B}} = \mathbf{0.45}\sigma \tag{4.6.2}$$

In this analysis, I examined eight variables to identify potential candidates for improving signal significance. To optimize our selections, I utilized the $\frac{S}{\sqrt{B}}$ formula, where $S$ represents the signal and $B$ represents the background. By applying a carefully chosen final cut based on the calculated signal significance, we successfully attained a final significance value of $0.45\sigma$.

Chapter 5

# Silicon Sensor for Outer Tracker of CMS

## 5.1 Sensor Design

By incorporating the Silicon Sensor into the outer tracker of the CMS (Compact Muon Solenoid), the $L_1$ trigger process will be greatly enhanced, while it will be able to withstand high levels of radiation and function effectively. Following these sections, we will discuss silicon strip sensor design components and the layout parameters associated with them.

### 5.1.1 General Design Elements

The signal to noise ratio of P-type material in silicon sensors surpasses that of N-type material after being exposed to radiation. Following irradiation, the N-type sensor displays non-Gaussian noise effects, which is why the P-type bulk region is preferred for the silicon sensor [43]. Below are some fundamental design elements associated with silicon sensors:

#### 5.1.1.1 Signal Coupling

When charged particles generate current signals at sensor electrodes, there are two possible methods for transmitting these signals to the readout electronics. In one approach, the amplifiers of the readout chip establish a direct connection with the sensor electrodes using a DC-coupled arrangement. Since charge carriers are moving as a result of the movement of the DC sensor, DC leakage current is transmitted along with the AC current signal. Identifying DC coupling is

relatively straightforward, particularly when dealing with a high sensor leakage current, since the amplifiers are required to handle a constant DC current component. Figure 5.1 illustrates DC coupling.

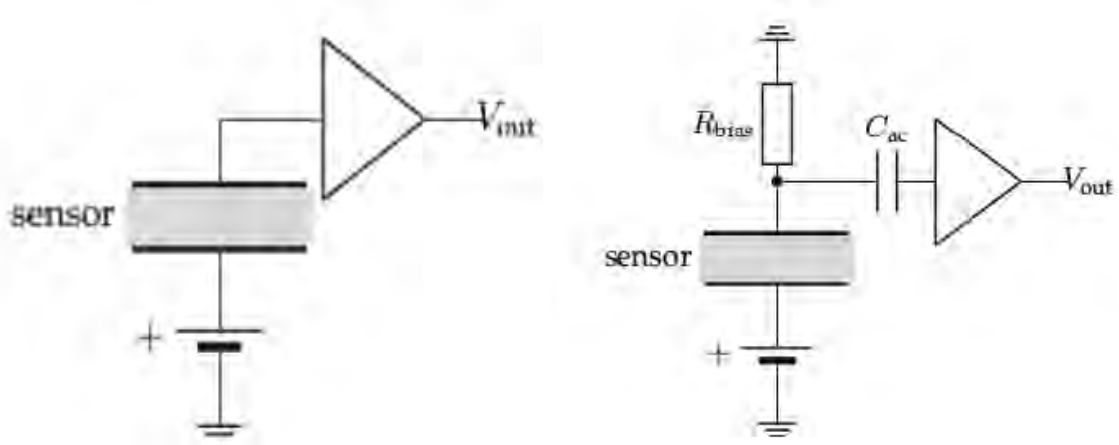


**Figure 5.1:** DC and AC coupled configuration of Silicon Sensor [22].

**In AC coupling**, the DC sensor bias and readout amplifiers are separated. AC current signals pass through coupling capacitance to reach the amplifiers, while DC current flows through bias resistance. $SiO_2$ serves as the dielectric material to block DC current between the n-type implant and the aluminum readout electrodes. The DC pads connects to the readout amplifier in the DC configuration, while the AC pad connects to the other electrode. Signal electrodes in silicon strip sensors are connected to the readout chip using wire bonds. Figure 5.1 shows AC coupling.

#### 5.1.1.2 Passivation

To protect the sensor from environmental radiation and provide electrical isolation, a passivation layer is applied on top of it. Silicon dioxide and silicon nitride are commonly used materials for passivation. The passivation layer includes strategically etched openings that allow for contact with the aluminum electrodes, enabling sensor readout, biasing, and electrical tests. By carefully placing these openings, the wire bonding path to the readout hybrids is kept short.

#### 5.1.1.3 Electrode Isolation

To ensure accurate position resolution, it is essential to achieve electrical isolation between individual sensor electrodes. This isolation needs to be maintained even after irradiation, ne-

cessitating initial resistances between the electrodes of greater than 10 GΩ. In the silicon dioxide layer, positive fixed charges attract minority carrier electrons from the p-type bulk towards the Si-$SiO_2$ interface. Consequently, the $n^+$ electrodes become effectively shortened, resulting in an electron accumulation layer on the sensor surface. By incorporating a p-stop implant between the $n^+$ implants, effective isolation can be achieved as shown in figure 5.2.

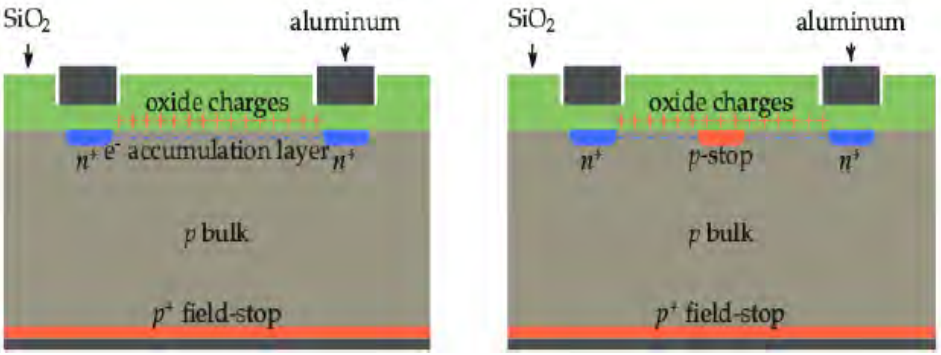


**Figure 5.2:** An illustration of an AC-coupled p-in-n sensor is depicted in a schematic cross-section, highlighting the concept of electrode separation [22].

#### 5.1.1.4 Sensor Bias

The required bias potential difference is applied between the front and back electrodes of a silicon sensor to deplete its active volume. The back-plane, connected to a high potential, includes a low resistivity $p^+$ doping region for a strong connection with the silicon substrate. This region, known as the "field-stop," prevents avalanche breakdown under high electric field conditions [44]. AC-coupled strip sensors commonly utilize polysilicon resistors to bias individual strips, connecting them to a shared $n^+$ bias line called the bias ring. The bias ring encircles the sensor's active region to justify a uniform potential across all strips. Poly-silicon resistance helps limit high leakage currents in individual strips following sensor irradiation as shown in figure 5.3.

#### 5.1.1.5 High Voltage Stability

A silicon sensor that operates at or above its full depletion voltage will guarantee a high signal-to-noise ratio. For the detector at the HL-LHC, which is nearing its end of its lifetime, operation voltages of more than 600 V is required. The sensors must maintain the required operating voltage without experiencing breakdown. It is common for the edges of sensors to be damaged and impurified during dicing, when the sensor is cut from the wafer, causing breakdown. An

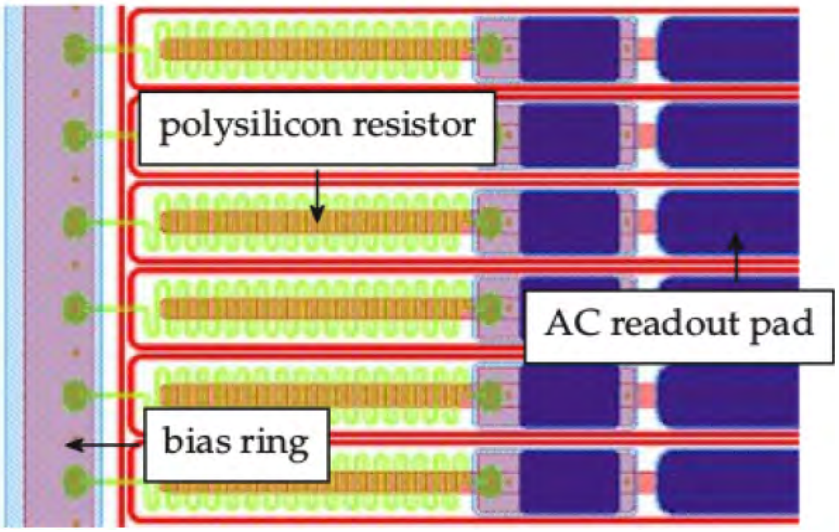


**Figure 5.3:** PS-s sensor with polysilicon resisters [23].

edge ring of $p^+$ implantation is applied to shield the edges from defects.

By doing so, the space charge region is prevented from reaching the defect by this edge ring. Additionally, the $p^+$ implantation stops surface current from flowing through the dicing region. An $n^+$ guard ring is positioned between the edge ring and the sensor's active region. The guard ring can be connected to ground potential to drain leakage current from the sensor's edge or left floating to create a lateral electric field, reducing the potential gradient at the sensor's periphery as shown in figure 5.4.

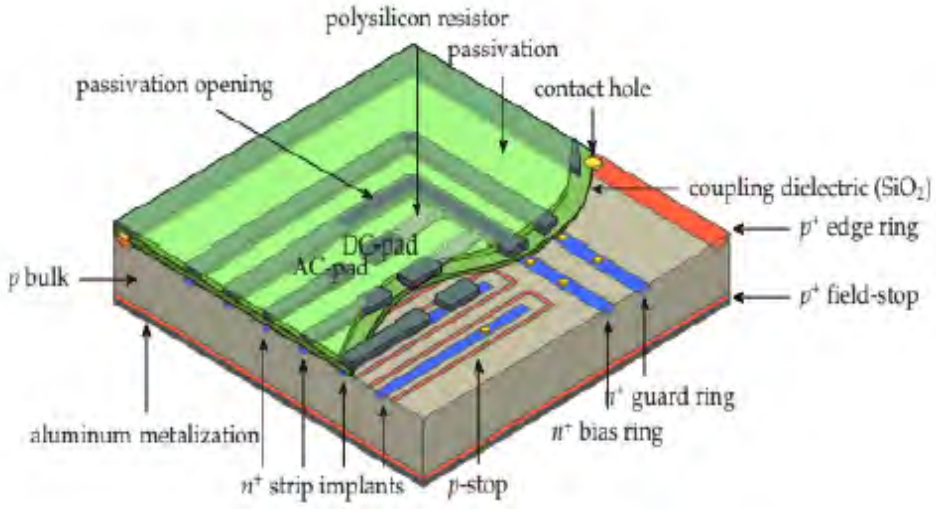


**Figure 5.4:** Design of a Three-Dimensional (3D) AC-Coupled n-in-p Silicon Strip Sensor [23].

## 5.2 Outer tracking sensors using silicon strips

In the CMS outer tracker, there are two components: the 2S module is located at the outer edge, and the PS module is located at the inner edge.

### 5.2.1 Characteristics of 2S and PS Sensors: 'Layout Parameters

The 2S sensor has a surface area of approximately $10 \times 10\,\mathrm{cm}^2$. It consists of 1016 parallel strips divided into two segments, each around 5 cm long, resulting in a total of 2032 channels. There is a 90 $\mu$m pitch for the 2S sensor. Meanwhile, the PS sensor has a surface area of approximately $10 \times 5\,\mathrm{cm}^2$. There are 960 parallel strips divided into two segments, each 2.5 cm long, resulting in a total of 2032 channels. The PS sensor has a pitch of 100 $\mu$m. PS and 2S sensors share the same peripheral layout. The active sensor region is surrounded by a 75 $\mu$m wide $n^+$ bias ring with asymmetric metal overhangs. The guard and edge rings have widths of 40 $\mu$m and 500 $\mu$m, respectively. All layout parameters for the outer tracker of the strip sensor are provided in Table 5.1.

**Table 5.1:** Measurement of the 2S Sensors in the Outer Tracker

| **Parameters** | **2S** |
|---|---|
| Dimension of Sensor | $102700\,\mu\mathrm{m} \times 94183\,\mu\mathrm{m}$ |
| Pitch between strips | $90\,\mu\mathrm{m}$ |
| Width of strip | $22.5\,\mu\mathrm{m}$ |
| $w/p$ ratio | 0.25 |
| Number of strips (2032) | $2 \times 1016$ |
| Length of single strip | 5 cm |
| Thickness of active sensor (ta) | $290\,\mu\mathrm{m}$ |
| Thickness of physical sensor (tp) | $320\,\mu\mathrm{m}$ |
| Bias ring width | $75\,\mu\mathrm{m}$ |
| Guard ring width | $40\,\mu\mathrm{m}$ |
| Edge ring width | $500\,\mu\mathrm{m}$ |
| Length of DC & AC Pad | $110\,\mu\mathrm{m}$ & $794\,\mu\mathrm{m}$ |
| Width of DC & AC Pad | $64\,\mu\mathrm{m}$ |

## 5.3 Radiation Damage in Silicon Sensor

In silicon sensors, two distinct types of damage can occur. The first type, known as bulk damage, arises from the permanent displacement of atoms from their original positions within the silicon material. On the other hand, surface damage occurs specifically in the insulator layers, such as $Sio_2$ (silicon dioxide), of the silicon sensor, and is caused by ionization effects.

### 5.3.1 Bulk Damage in Silicon Sensors

Radiation damage in the bulk of silicon sensors primarily occurs due to elastic collisions between heavy particles and the atomic nuclei of crystal lattice. These collisions can result in the displacement of individual atoms, leading to the formation of point defects, or can trigger a cascade of dislocations that form cluster defects. When an atom is displaced, it creates a silicon interstitial and leaves behind a vacancy, forming a defect known as a Frankel pair. Figure 5.5 illustrates a Frankel defect. Displacement of an atom depends on the material's binding forces.

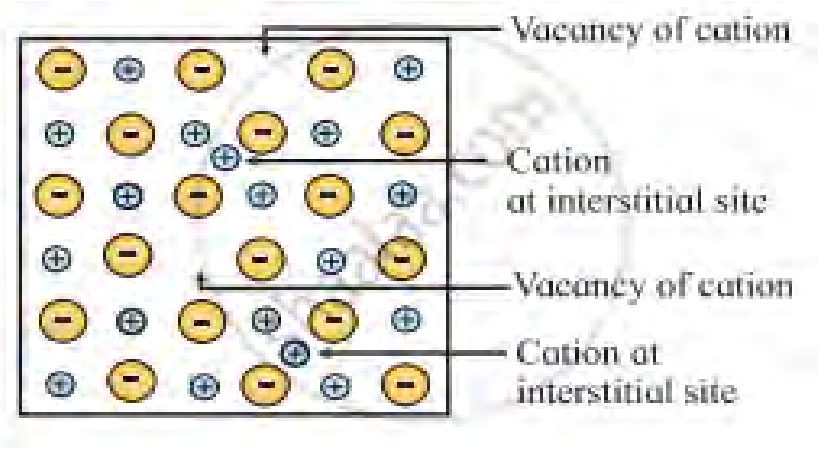


**Figure 5.5:** Vacancy and interstitial in the silicon lattice ("Frenkel defect") [24].

The table 5.2 provides a summary of the main properties associated with point defects and cluster defects. Here is how displacement damage is expressed:

$$D(E) = \sum \delta_i(E_{\text{kin}}) \int_0^R Z R_0 f_i(E_{\text{kin}}, E_R) P(E_R)\, dE_R \tag{5.3.1}$$

The cross-sectional area of a process, denoted as $\delta_i$, is related to the Lind-hard partition function $P(E_R)$, which represents the energy required to displace an atom in silicon. $E_R$ represents the recoil energy, and $f_i$ represents the probability of collision with other particles having kinetic energy $E_{\text{kin}}$. P(E) values for different particles, including 10 MeV proton, 24 GeV proton, and

**Table 5.2:** Minimum Kinetic Energies for Defect Formation by Different Particles

| **Particle** | **Defect Type** | **Minimum Energy** |
|---|---|---|
| Neutron | Single Point Defect | 10 MeV |
| Neutron | Cluster Defect | 100 MeV |
| Proton | Single Point Defect | 100 MeV |
| Proton | Cluster Defect | 1 GeV |
| Electron | Single Point Defect | 1 MeV |
| Electron | Cluster Defect | 10 MeV |
| Co-gammas | Single Point Defect | 1 keV |
| Co-gammas | Cluster Defect | 10 keV |

1 MeV neutron, are 50%, 42%, and 43%, respectively. The NIEL hypothesis can be used to scale the damage caused by these particles [45]. It involves scaling the fluence of any particle to an equivalent fluence $\Phi_{eq}$ of mono-energetic 1 MeV neutrons, this would result in damage the sensor. This scaling can be expressed as follows:

$$\Phi_{eq} = \kappa \cdot \Phi \tag{5.3.2}$$

Here, $\Phi_{eq}$ represents the equivalent fluence of mono-energetic 1 MeV neutrons, $\Phi$ represents the fluence of the particle being considered, and A particle's hardness factor is $\kappa$, which indicates the extent of its damage.

#### 5.3.1.1 Impact of Radiation on Sensor Properties

In addition to causing a reduction in charge collection efficiency, radiation-induced bulk damage results in an increase in leakage current and depletion voltage.

**Effects of Leakage Current**

Radiation exposure causes the generation of mid-gap defects, which efficiently produce electron-hole pairs, leading to increased leakage currents. Several experiments have demonstrated a linear relationship between dark current and fluence, resulting in elevated noise levels. This relationship can be described by the equation:

$$\Delta I = \alpha \phi_{eq} V \tag{3.2.3}$$

Here, $\alpha$ represents the damage rate related to current, and V denotes the normalized volume.

### Depletion Region

The irradiation process introduces accepter-like and eliminates donor-like states, impacting shallow defects in the semiconductor material. Until the inversion point, when n-type silicon turns into p-type, this alteration results decrease in effective doping concentration. As soon as the effective doping concentration reaches the inversion point, the full depletion voltage increases. In n-type sensors, the space charge region expands from the other side after irradiation, prohibiting operation below the full depletion voltage.

Contrary to p-type materials, they do not exhibit an inversion point, so the voltage of full depletion is not affected. Higher radiation levels lead to increased full depletion voltage, posing challenges for sensor power supply and necessitating cooling techniques to reduce power loss as illustrated in figure 5.6.

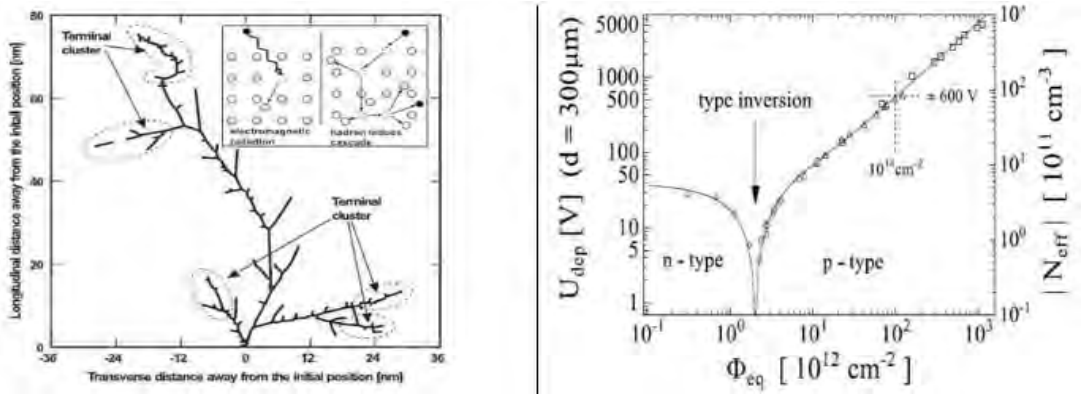


**Figure 5.6:** (a) Cluster damage and atomic displacement model due to electromagnetic radiation and heavy particle impact. (b)Voltage and effective doping changes during full depletion of a 300 $\mu$m thick silicon sensor with normalized fluence after irradiation [25].

### Effects of Charge Trapping

Deep levels having longer de-trapping times compared to detector electronics have a detrimental impact. This results in weakened signals, loss of charge, and a decline in charge collection efficiency. Defects within the material can trap either electrons or holes. The following observations have been made regarding the impact of bulk damage on sensor properties:

- The leakage current increases at $10^{14}$ $n_{1MeV}/cm^2$.

- The depletion voltage rises at $10^{15}$ $n_{1MeV}/cm^2$.

- The charge collection efficiency degrades at $10^{16}$ $n_{1MeV}/cm^2$. figure below 5.7 explain this phenomenon.

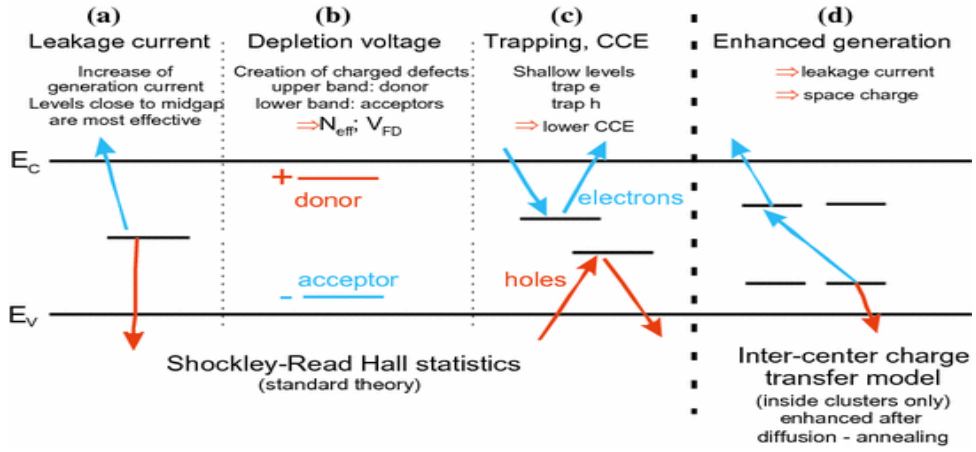


**Figure 5.7:** Exploring Defect Level Positions and their Impact [25].

### 5.3.2 Surface Damage

Damage to the surface is primarily caused by ionization in the insulating layer $Sio_2$ rather than atomic displacement in the silicon bulk of a silicon sensor. Photon and charged particle interactions generate electron-hole pairs within the $Sio_2$ layer, although these pairs are not fully reversible in the insulator. Electron mobility is higher than hole mobility in the oxide. In turn, electrons are driven towards metal electrodes while holes are trapped at Si-$Sio_2$ interfaces. As shown in figure 5.8, the positive oxide charges (holes) attract minority electrons from p-type sensors, increasing noise due to increased inter-strip capacitance and reduced inter-strip resistance.

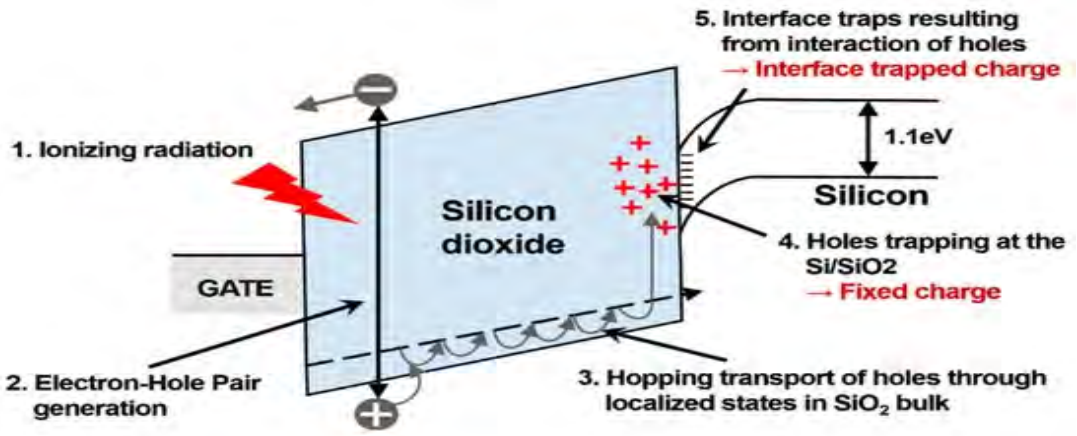


**Figure 5.8:** Effects of Radiation on the Si-$SiO_2$ Interface [26].

Chapter 6

# Qualifying and Characterizing Silicon Sensor for CMS Outer Tracker

The Sensor Quality Control (SQC) procedure ensures that a set of sensors meets specifications before integration into CMS tracker modules. SQC involves characterization and evaluation to verify compliance. Their important tasks are given below:

**Visual Assessment**: Following removal from the packaging, each sensor designated for characterization must undergo immediate inspection using a suitable microscope. The entire length of the dicing cut and the sensor's perimeter should be carefully examined for potential damage, including chips, fractures, scratches, stains, or residue.

**Electrical Evaluation**: The subsequent section presents a discussion on the electrical testing setup employed by SQC for characterizing silicon sensors.

## 6.1 Electrical Testing setup for SQC

The SQC setup is utilized to measure both global parameters and strip parameters of 2S silicon sensors. Global parameters include leakage current versus reverse bias voltage (IV) and bulk capacitance versus reverse bias voltage (CV). On the other hand, strip parameters encompass coupling capacitance (CC), current through strip $I_{\text{strip}}$, poly-silicon resistance ($R_{poly}$), inter-strip resistance ($R_{int}$), dielectric current ($I_{diel}$), and inter-strip capacitance ($C_{int}$).

### 6.1.1 LCR Meter E4980A

An LCR meter is a device utilized for measuring inductance (L), capacitance (C), and resistance (R). The E4980A LCR meter having frequency range of 20 Hz to 2 MHz and can simultaneously measure DC voltage and current. CV, CC, and $C_{int}$ measurements are carried out using the LCR meter.

### 6.1.2 SMU 2636B

The SMU 2636B devices are employed for measuring and sourcing current-voltage. They have voltage and current ranges of 1 $\mu$V to 200 V and 1 fA to 10 A, respectively. Additionally, these devices are utilized for biasing silicon sensors.

### 6.1.3 Electrometer 6517B

The 6517B electrometer is utilized for highly precise current measurements. It offers current and voltage ranges of 100 A to 200 mA and 10 $\mu$V to 1000 V, respectively. Additionally, it can measure resistance within the range of 100 Ω to 10 pΩ. The electrometer is employed for determining inter-strip resistance and strip current.

### 6.1.4 Switch Matrix 707B

In switch matrix systems, any column can be connected to a single row, allowing for versatile signal routing between equipment and the device under test. These systems are commonly used for switching multiple channels. The 707B mainframe can control six 8x12 matrix cards. The two-dimensional framework consists of N rows and M columns, representing an arrangement of N times M values, Figure 6.1 below shows all equipment's.

### 6.1.5 Automated Probing System

Testing silicon sensors with a large number of strips necessitates an automated probe system. The renowned MPI TS2000 Probe System is designed for advanced semiconductor testing, featuring a Poly tetra fluoroethylene based vacuum chuck (PTFE) with XYZ movement (210 mm × 340 mm × 10 mm) to securely position the sensor. Optical inspection is performed using a microscope, while temperature and humidity are controlled. Electrical characterization

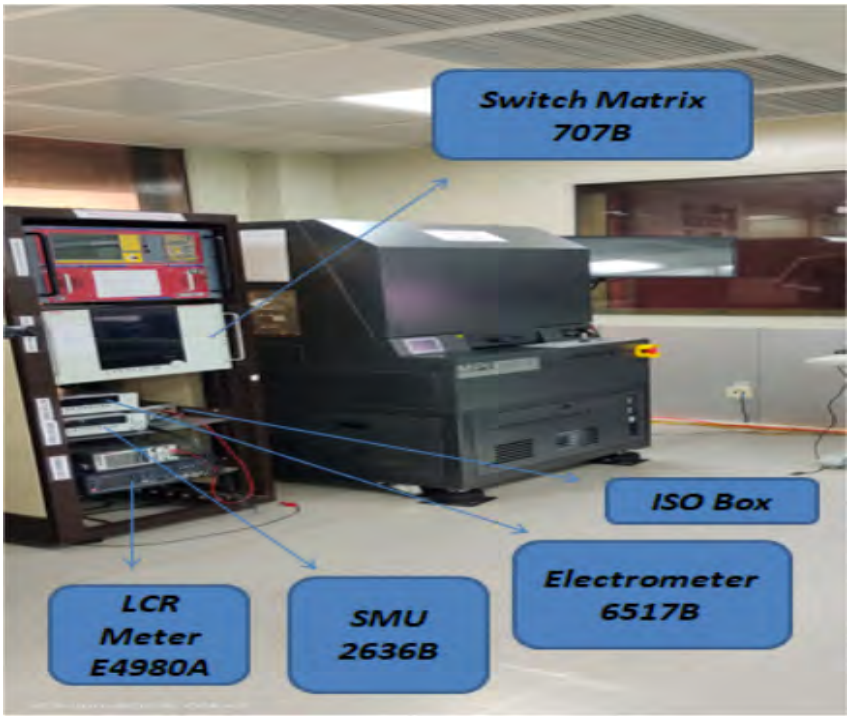


**Figure 6.1:** Electrical Setup for SQC at the EHEP Lab, NCP

employs a probe needle connected to SMU, LCR, or Switch Matrix. A custom Lab-View-based software and Python script analyze and present the measurement data. The sensor is placed in the probe station chuck, aligned, and the bias needle is fixed onto it. Figure 6.2 explain the SQC Phenomenon. Capture snapshots from various positions during visualization. Connect the DC1

**Figure 6.2:** Functional Sensor Placement on Chuck vs. Optical Sensor Inspection

needle to the sensor's DC pad and the AC1 needle to the sensor's AC pad. Monitor the internal humidity until it reaches 10%. Begin by measuring the global parameters and then proceed to measure the strip parameters. Figure 6.3 show the Prob station and PC running lab-View.

A total of eight parameters are evaluated to qualify the 2S silicon sensor, encompassing both


**Figure 6.3:** In the cleanroom at NCP, utilize the Probe System and PC running Lab VIEW.

global and strip parameters, as detailed in the following section.

## 6.2 Global Parameters measurements

Global parameters include the relationship between leakage current and reverse bias voltage, as well as the correlation between bulk capacitance and reverse bias voltage.

### 6.2.1 Leakage Current vs Reverse bias voltage

The current generated by minority charge carriers in a semiconductor is referred to as leakage current ($I_{\text{leakage}}$). Minimizing leakage current is crucial as it serves as a source of noise. It is proportional to depletion region width ($w$), which in turn is proportional to $\sqrt{V_{\text{bias}}}$. Ideally, leakage current should remain constant when the external bias voltage is equal to the full depletion voltage. Bulk leakage currents are influenced by temperature. The mathematical formula for the heating power of a silicon sensor can be represented as:

$$P_{\text{bias}} = V_{\text{bias}} \times I_{\text{leakage}} = V_{\text{bias}} \times T^2 \times e^{-\frac{E_{\text{eff}}}{2k_B T_{\text{silicon}}}} \tag{6.2.1}$$

The current between the bias ring and the backplane is measured as a function of the reverse bias voltage. The voltage range for measurement is 0-1000 V, with the backside set to a negative

potential and the frontside maintained at ground potential. The SMU 2636B instrument was utilized for the source and current-voltage measurements. This IV connection diagram 6.4 taken from SQC spec document [1]. Figure 6.5 shows the plots of IV of different 2S sensors,

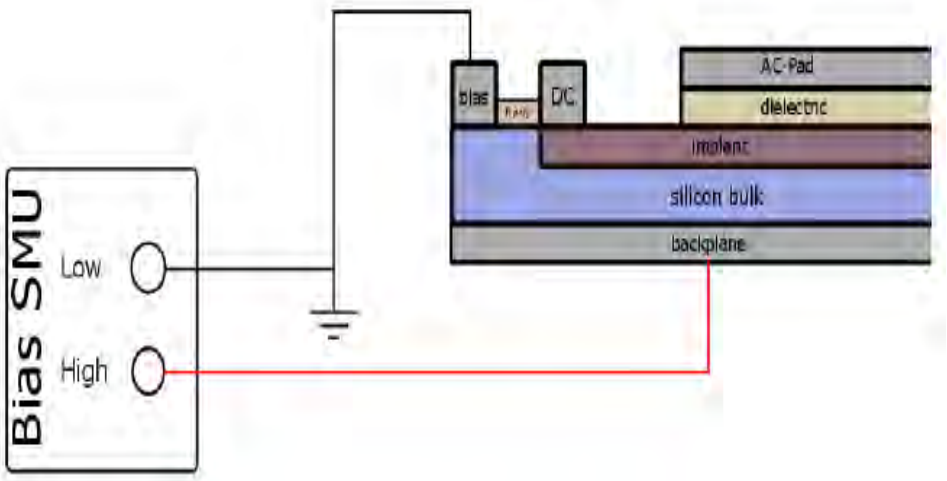


**Figure 6.4:** SQC specification document shows IV connection diagram [1]

.

batch 43264. Increasing the reverse bias voltage can result in an expansion of the depletion

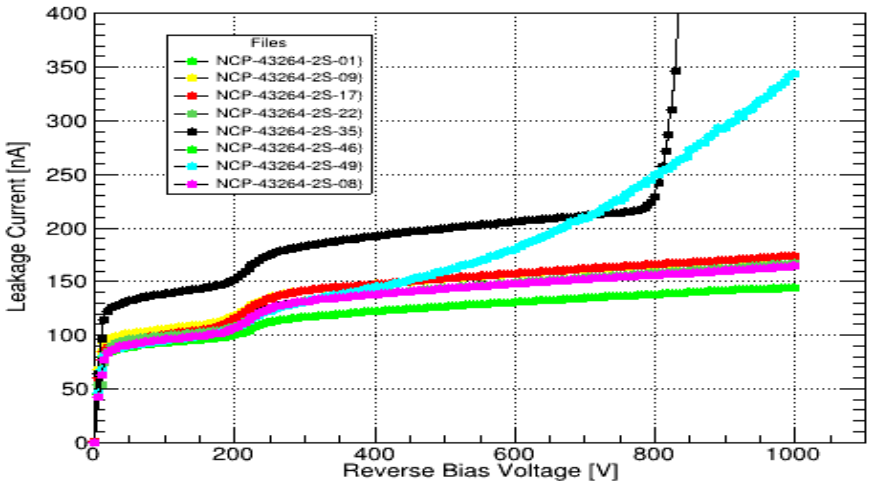


**Figure 6.5:** Leakage current vs reverse bias voltage.

region within the silicon sensor, leading to an increase in leakage current. However, at a certain voltage, the leakage current tends to remain approximately constant. Further increasing the voltage beyond this point may cause an avalanche effect. When the breakdown voltage is reached, the sensor becomes damaged. Several factors can contribute to an increase in leakage

current, such as temperature, relative humidity, doping concentration, and bulk defects. The specified range for leakage current is 7.5 $\mu$A, and the breakdown voltage should exceed 800 V. When measuring the average leakage current values for sensors 38714_2$S$-019, 38714_2$S$-023, and 38714_2$S$-037 at 600 V, the recorded values were $-128.7$ nA, $-133.4$ nA, and $-115.9$ nA respectively, which all fall within the acceptable range.

### 6.2.2 Bulk Capacitance vs Reverse Bias Voltage

A reverse bias voltage is used to measure the capacitance between the back and front plane. The frontside will remain at ground's potential, while the backside should be at negative potential according to CV range. The CV range is from 0 to 600 V. The bulk capacitance versus reverse bias voltage was measured using SMU 2636B, an ISO box, and an LCR meter E4980A. Figure

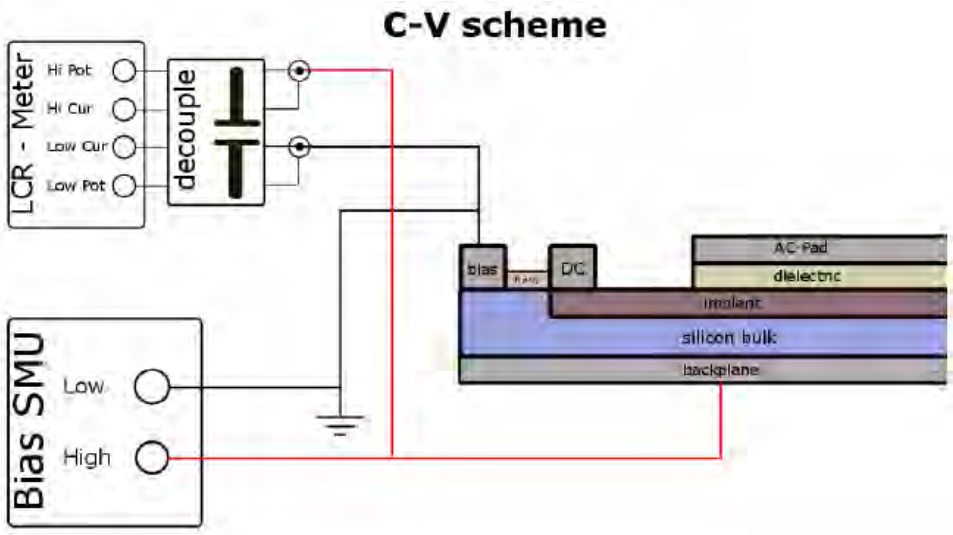


**Figure 6.6:** SQC specification document shows IV connection diagram [1].

6.6 and 6.7 shows connection diagram and CV plots for different 2S sensors, batch 43264. When we increase voltage, we see that the bulk capacitance decreases. At a certain voltage, the bulk region becomes fully depleted; this is known as the "full depletion voltage". Since the depletion layer acts like a parallel plate capacitor, its bulk capacitance per unit area is:

$$C_{\text{bulk}} = \epsilon_0 \epsilon_{\text{si}} / w \tag{6.2.2}$$

The width of depletion layer is given by w, where

$$w = \sqrt{2\epsilon_0 \epsilon_{\text{si}} \mu \rho |V_{\text{bias}}|} \tag{6.2.3}$$

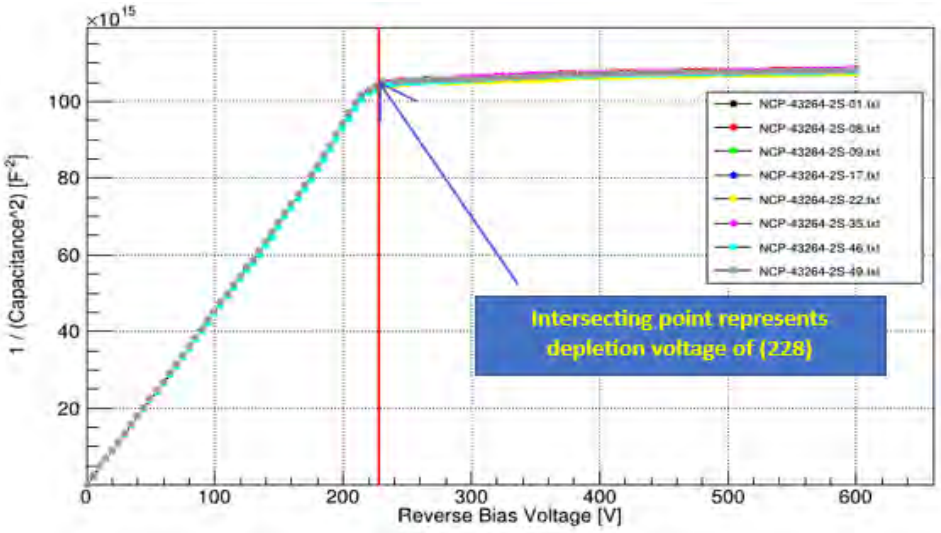


**Figure 6.7:** Capacitance vs reverse bias voltage.

$V_{bias}$ relates to reverse bias voltage, $\mu$ is the mobility of the majority charge carrier and $\rho$ is the specific resistance.

$$\rho = \frac{1}{e\mu N_{\text{eff}}} \tag{6.2.4}$$

In the equation above 6.2.2 , we can get the full depletion voltage which is given below.

$$V_{\text{FD}} = \left| \frac{N_{\text{eff}} q D^2}{2\epsilon_0 \epsilon_{\text{si}}} \right| = \frac{D^2}{2\epsilon_0 \epsilon_{\text{si}} \mu \rho} \tag{6.2.5}$$

Full depletion voltage depends on sensor thickness (D) and material resistivity (R). High resistivity materials (low doping) require low depletion voltages because they have low depletion voltages in bulk.

The range of full depletion voltage $< 360$ V. I have measured an average full depletion voltage of 260 V for the sensors 43264_2S-035, 43264_2S-046 and 43264_2S-049. A sensor with a high full depletion voltage may degrade due to defects. For $V_{\text{bias}}$ VFD, silicon sensors have the following bulk capacitance:

$$C_{\text{bulk}} = \sqrt{\frac{\epsilon_0 \epsilon_{\text{si}}}{2\rho\mu V_{\text{bias}}}} \tag{6.2.6}$$

As a result of these factors, the bulk capacitance of silicon sensors for $V_{\text{bias}} \geq$ VFD is:

$$C_{\text{bulk}} = \frac{\epsilon_0 \epsilon_{\text{si}}}{D} \tag{6.2.7}$$

Accordingly, all factors in equation remain constant in equation 6.2.7, and capacitance remains constant with increasing reverse bias voltage. In table 6.1 I report the measured values of global parameters for 2S sensors. My measured values of global parameters for 2S sensors are given in table 6.2.

**Table 6.1:** A global set of parameters that qualify 2S sensors.

| **Electrical Parameter** | **Range** |
|---|---|
| IV range, $V_{\text{IV range}}$ | 0 - 1000 V |
| IV step size, $V_{\text{IV step}}$ | 5 V |
| IV min. delay, $t_{\text{IV}}$ | 500 ms |
| CV range, $V_{\text{CV range}}$ | 0 - 600 V |
| CV step size, $V_{\text{CV step}}$ | 5 V |
| CV min. delay, $t_{\text{CV}}$ | 500 ms |
| Full depletion voltage, $V_{\text{fd}}$ | $< 350$ V |
| Current at 600V, $I_{600}$ | 7.25 $\mu$A |
| Breakdown voltage, $V_{\text{break}}$ | $> 800$ V |

**Table 6.2:** Measured average values of global parameters of the 2S sensor for batch 43264

| Sensor No | $I$@600 (nA) | I @800 (nA) | I 800/I 600 (nA) | $V_{fd}$ |
|---|---|---|---|---|
| 38714_2S_019 | −130.87 | -138.39 | -1.057 | 228 |
| 38714_2S_023 | −122.17 | -129.87 | -1.063 | 228 |
| 38714_2S_037 | −170.27 | -180.69 | -1.061 | 228 |

## 6.3 Strip Parameters

The strip parameters include coupling capacitance, strip current, poly-silicon resistance, inter-strip resistance, dielectric current, and inter-strip capacitance.

### 6.3.1 Inter-strip Resistance

An interstrip resistance is measured between the DC pads having adjacent strips. A small voltage ramp of 5 V is used to measure the current. Inter-strip resistance can be calculated easily from the inverse slope of the ramp. $R_{\text{int}}$ result will be considered linear if it shows linear behavior. A connection diagram for the SMU 2636B and 2470 was used during the measurement of inter-strip resistance between two strips. The plots and connection diagram of $R_{\text{int}}$ for different 2S sensors, batch 43264 are given in figure 6.8 and 6.9. In order to isolate silicon sensor strips, a higher inter-strip resistance is needed. $R_{\text{int}} > 10$ $G\Omega$ is measured in G$\Omega$. $R_{\text{int}}$ can be measured between individual strips if there is no inter-strip resistance due to

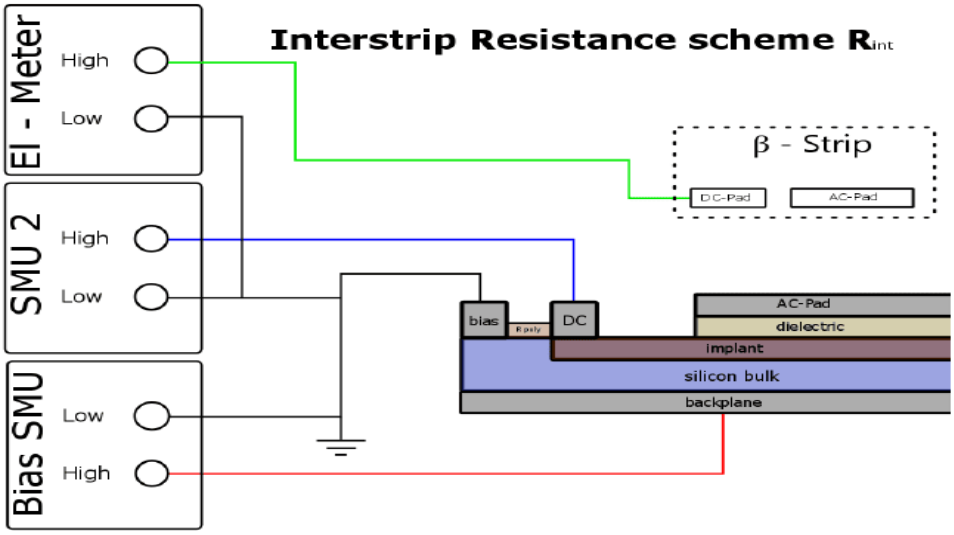


**Figure 6.8:** SQC specification document shows $R_{int}$ connection diagram [1].

damage. If there is no inter-strip resistance, $R_{\text{int}}$ will be low. The values which I measured for R-int for NCP-43264-2S-35, NCP-43264-2S-46, NCP-43264-2S-49 sensors are 187.89 GΩ, 194.00 GΩ and 185.49 GΩ, which are in accepted range.

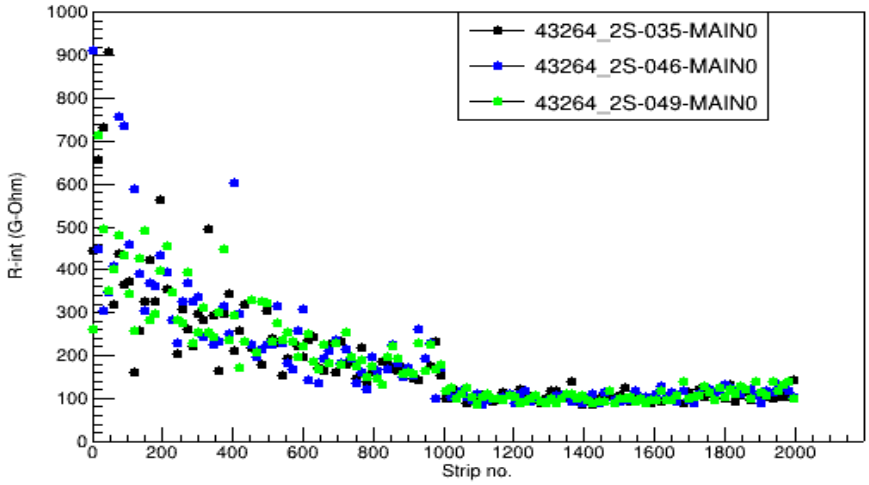


**Figure 6.9:** R-int vs strip number.

### 6.3.2 Poly-silicon resistance

A small voltage of 5 V is applied between the bias ring and DC pad, and a current is measured. For the calculation of polysilicon resistance, we have

$$R_{\text{poly}} = \frac{V_{\text{poly}}}{I_{\text{strip}}} \tag{6.3.1}$$

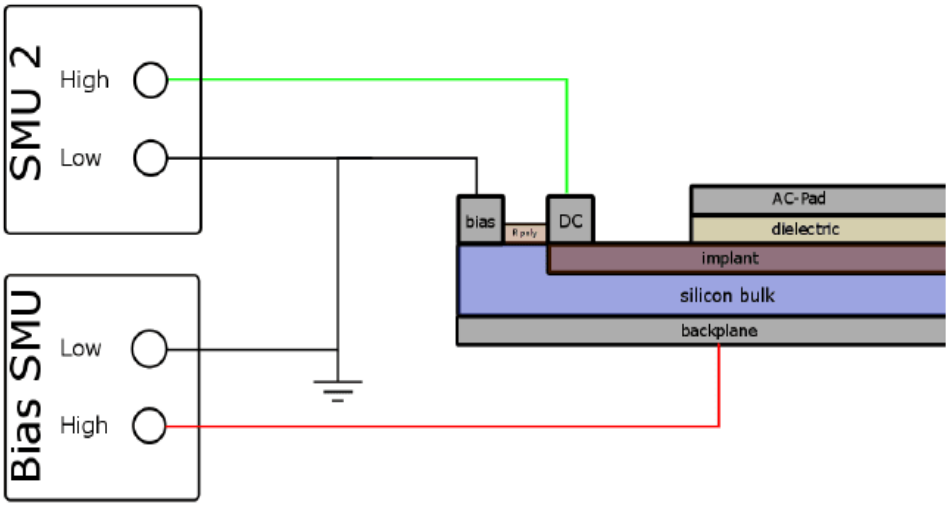


**Figure 6.10:** SQC specification document shows connection diagram for $R_{\text{poly}}$ [1].

Connection diagram for $R_{\text{poly}}$ is given in figure 6.10. The plots which I made for $R_{\text{poly}}$ of different 2S sensors, batch 43264 are given in figure 6.11. The noise is related to the poly-silicon resistance as $\sqrt{\frac{K_B T}{R_{\text{poly}}}}$, where KB is the Boltzmann constant, T represents temperature, and $R_{\text{poly}}$ denotes the poly-silicon resistance. Therefore, a high resistance value is desired for low noise. The values which I measured for R-int for NCP-43264-2S-35, NCP-43264-2S-46, NCP-43264-2S-49 sensors are 1.45 MΩ, 1.43 MΩ and 1.44 MΩ

### 6.3.3 Strip Current

Using SMU 2636B and 2470 meters, I measured strip current between the DC pad and external ground source. The connection diagram and plots for strip current are given in figure 6.12 and 6.13, where Strip number is on the X-axis and strip current is on Y-axis. The strip current range is less than 50 nA. Increased strip current results in an increase in noise. My measured average values of strip current for NCP-43264-2S-35, NCP-43264-2S-46, NCP-43264-2S-49 sensors are -50.72 pA, -60.89 pA and -60.85 pA respectively which are in accepted range.

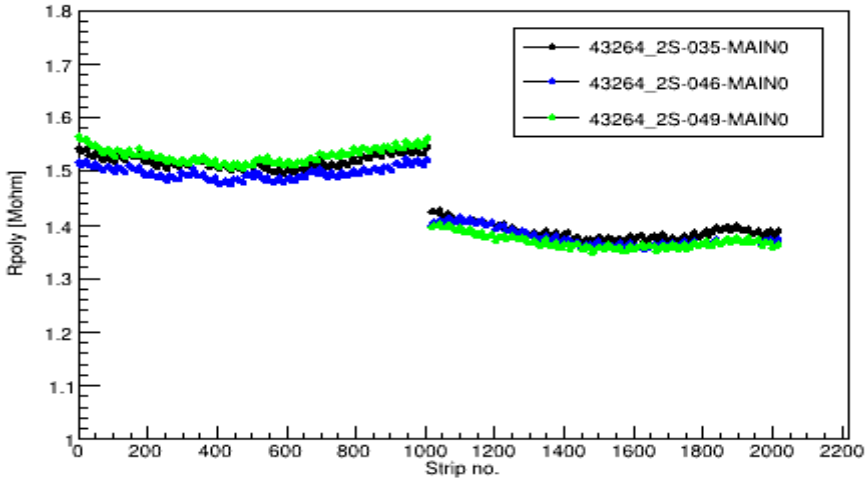


**Figure 6.11:** $R_{\text{poly}}$ vs strip number.

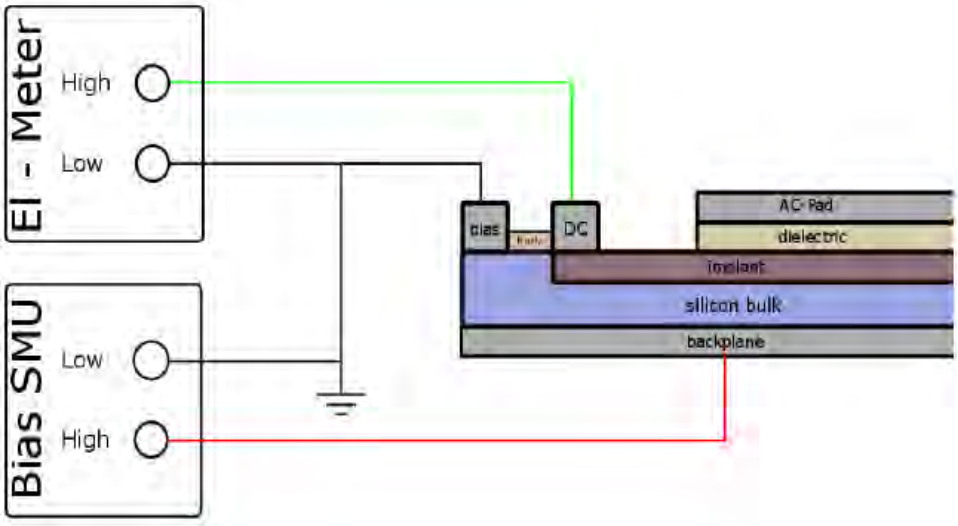


**Figure 6.12:** SQC specification document shows $I_{strip}$ connection diagram [1].

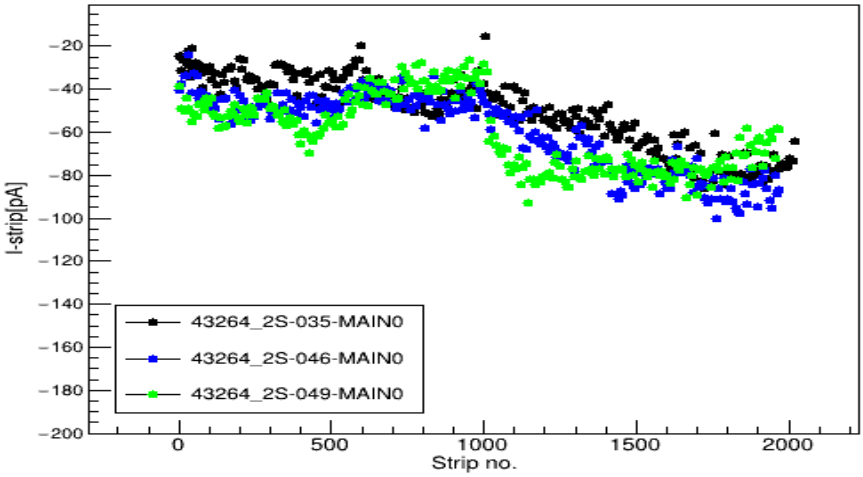


**Figure 6.13:** $I_{\text{strip}}$ vs strip number.

### 6.3.4 Dielectric Current

Through the dielectric $SiO_2$, small current measured across the AC and DC pads of the strip implant using a voltage of 10 volts. The high dielectric current indicates a pinhole. I used SMU 2636B and SMU 2470 meters to measure the dielectric current. Its connection diagram shows in figure 6.14. In plots of dielectric current 6.15, strip number is on X-axis and dielectric

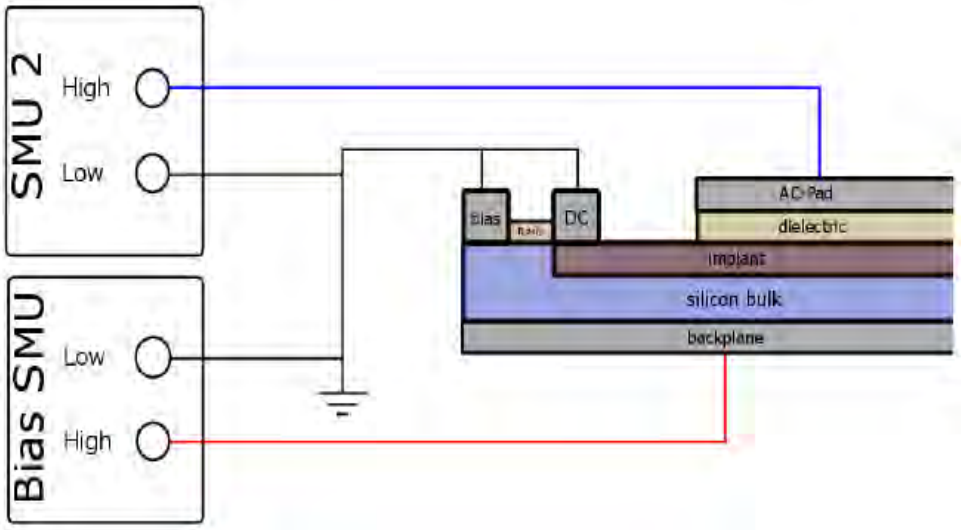


**Figure 6.14:** SQC specification document shows $I_{dielectric}$ connection diagram [1].

current is on Y-axis. Accepted range is $< 10$ nA. In the presence of pinholes, $I_{\text{diel}}$ will be measured in mA. The average values of dielectric current for NCP-43264-2S-35, NCP-43264-2S-46, NCP-43264-2S-49 sensors are 0.37 pA, 0.10 pA and 0.39 pA respectively which are in

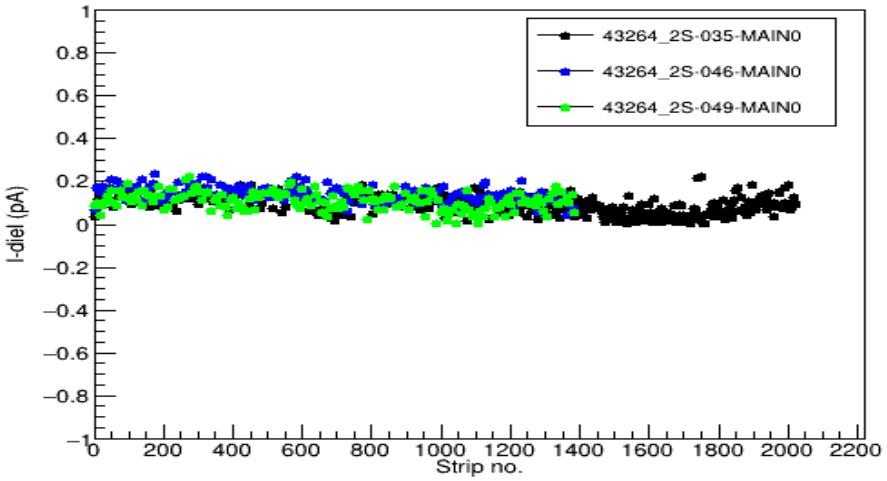


**Figure 6.15:** $I_{\text{dielectric}}$ vs strip number.

accepted range.

### 6.3.5 Coupling Capacitance

There is a coupling capacitance between the AC pad and the DC pad due to the dielectric $SiO_2$. Coupling capacitance is directly proportional to the signal, so it should be large in comparison to inter-strip capacitance. In order to achieve a large capacitance, an aluminum readout strip and implant strip are separated by a thin dielectric layer of 200 nm. Due to the ohmic connection

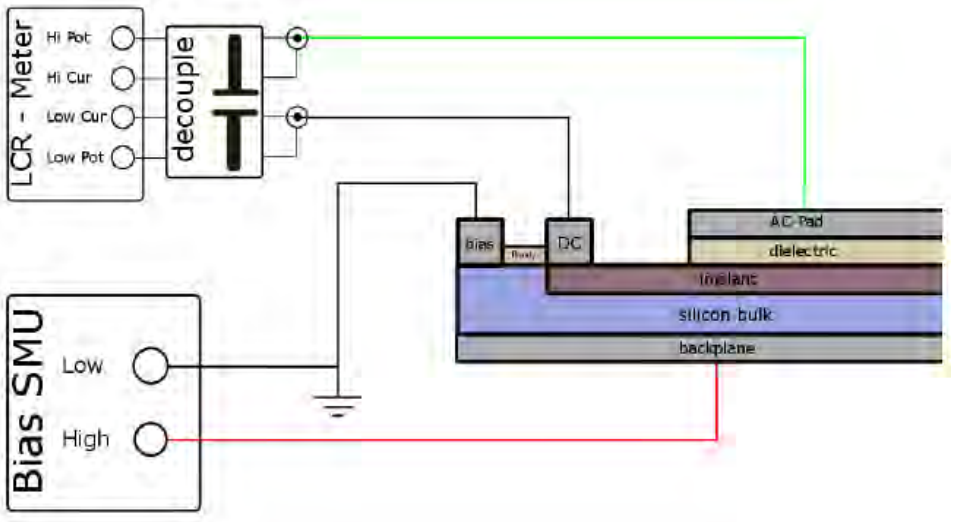


**Figure 6.16:** SQC specification document shows CC connection diagram [1].

between the aluminium readout strip and implant strip, the AC design was bypassed. As a

result, the preamplifiers will be overloaded and damaged. I measured coupling capacitance between the AC and DC pads with a LCR meter E4980A. The connection diagram and plots

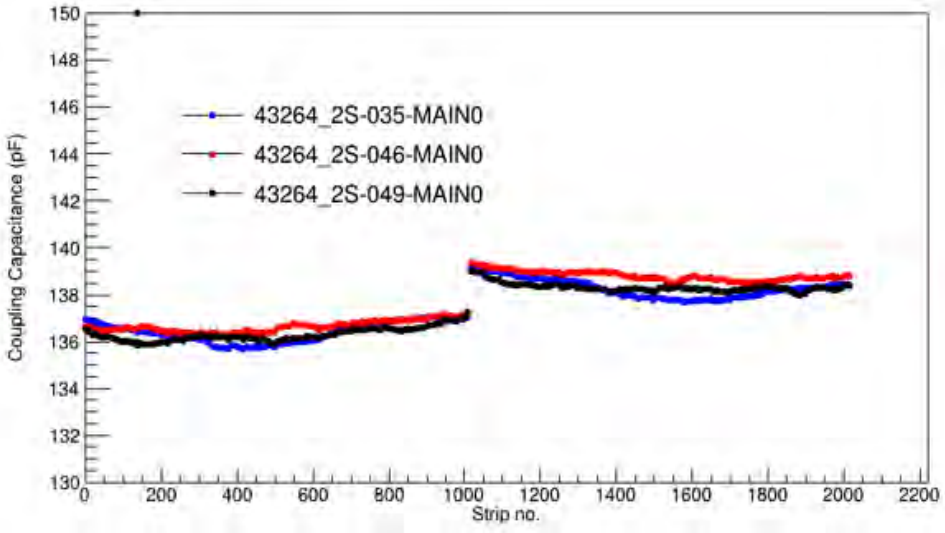


**Figure 6.17:** Coupling capacitance vs strip number.

of CC of different 2S sensors, batch 43264 are given figure 6.16 and 6.17. The range of CC is greater than 132 pF. My measured average values of coupling capacitance for sensors NCP-43264-2S-35, NCP-43264-2S-46, NCP-43264-2S-49 sensors are 142.9 pF, 142.8 pF and 143.1 pF respectively which are in accepted range.

### 6.3.6 Inter-strip Capacitance

The DC pads of the adjacent strip serve as a dielectric material in inter-strip capacitance. Inter-strip capacitance was measured using an LCR metre E4980A, SMU 2636B, and ISO box. For the purpose of testing inter-strip capacitance, just a sample of strips was employed. After every 15 strips, the $C_{\text{int}}$ value was calculated. The connection diagram and plots of Cint of different 2S sensors, batch 43264 are given in figure 6.18 and 6.19. There's a strip number on the X-axis and an interstrip capacity on the Y-axix. An inter-strip resistance has to be a certain value so that charge can be shared. The inter-strip capacitance must smaller than the coupling capacitance which gives better signal into the preamplifier. The range of $C_{\text{int}}$ is 2 pF. My measured average values of inter-strip capacitance for sensors NCP-43264-2S-35, NCP-43264-2S-46, and NCP-43264-2S-49 sensors are 1.58 pF, 1.58 pF and 1.57 pF which are in accepted range. The table 6.3 in the SQC specification document provides the specified ranges of strip parameters for 2S sensors. My results are shared at conclusion chapter at the end.

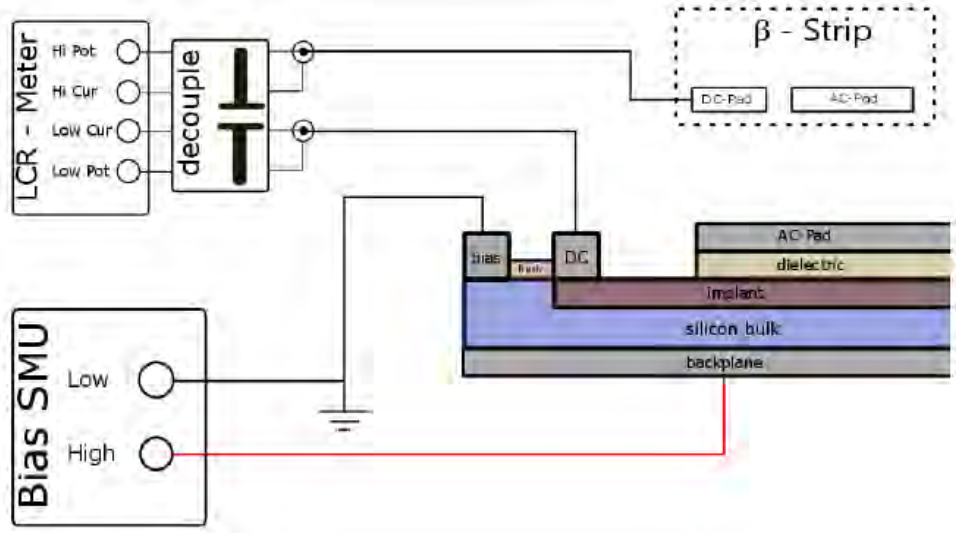


**Figure 6.18:** SQC specification document shows $C_{int}$ connection diagram [1].

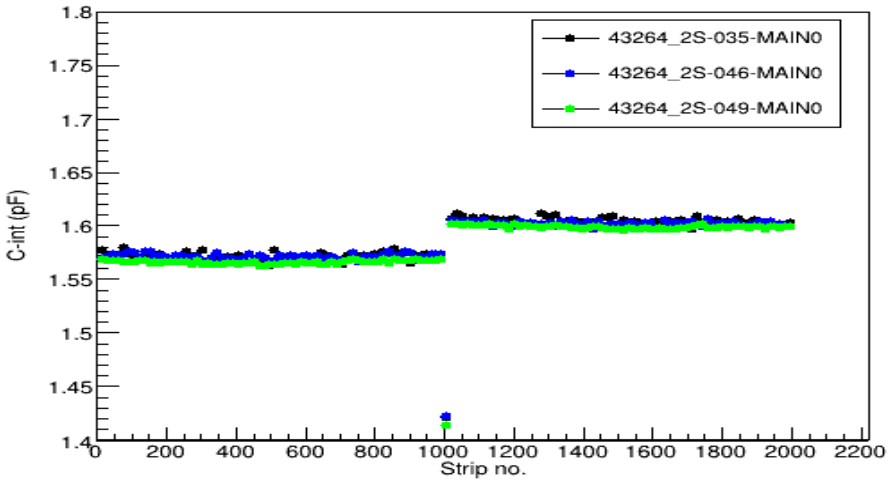


**Figure 6.19:** SQC specification document shows $C_{int}$ connection diagram.

**Table 6.3:** The qualification of 2S sensors involves determining the acceptable ranges for strip parameters.

| Electrical Parameters | Ranges |
|---|---|
| Strip current, $I_{\text{strip}}$ | $< 50$ nA |
| Bias resistance, $R_{\text{poly}}$ | $1.5 \pm 0.5$ MΩ |
| Coupling capacitance, $C_{\text{c}}$ | $> 132$ pF |
| Dielectric current, $I_{\text{diel}}$ | $< 10$ nA |
| Interstrip resistance, $R_{\text{int}}$ | $> 10$ GΩ |
| Interstrip capacitance, $C_{\text{int}}$ | $< 0.5$ pF/cm |
| Bias voltage for resistor, $V_{\text{poly}}$ | $< 5$ V |

Chapter 7

# Conclusion

As Standard Model of particle physics does not provide information about Dark Matter candidates. To explore Dark Matter interactions, new physics models beyond the Standard Model are required. Colliders like the LHC offer the opportunity to produce and study Dark Matter by observing its interactions with SM particles. Higgs boson discovery at LHC has opened up new possibilities for investigating the interaction between Dark Matter and the Higgs boson through the weak force. This thesis presents an analysis of Dark Matter particles produced in an association with Higgs boson. Based on simulated proton-proton collision data generated by MadGraph5_aMC@NLO at $\sqrt{s} = 13.6$ TeV, the feasibility studies are performed.

In the first part of my thesis, I focused on the decay of the Z boson into two oppositely charged leptons accompanied by a significant amount of missing transverse energy produced by Dark Matter particles. This search, known as the "mono-Z" search, offers advantages despite its lower cross-section compared to the mono-jet channel. In this analysis, I studied the Two Higgs Doublet Model extended by a light pseudoscalar (referred to as "2HDM+a") as a benchmark model. Specifically, we examined the $Z \rightarrow \ell^+ \ell^-$ decay channel, where a heavy neutral Higgs decays into a Z boson and a pseudoscalar 'a', and the pseudoscalar 'a' further decays into a pair of Dark Matter particles ($a \rightarrow \chi\chi$). I used cut optimization for feasibility study of Dark Matter. To gain deeper insights into the process, I employed various criteria to distinguish the desired signal from background noise. This involved analyzing crucial kinematical variables like ($E_T^{miss}$), angular separations ($\Delta R$), ($\Delta\phi$), invarient mass (M), pseudorapidity ($\eta$), azimuthal angle ($\phi$) and scalar sum of momenta ($HT$) of final state particles which are leptons. I assessed the significance of each variable independently and, in the final stages, evaluated the overall significance by applying conclusive criteria to all cut variables. The signal's potency was quantified

using the formula $S/\sqrt{B}$, resulting in $0.45\sigma$. Table 7.1 shows summary table.

**Table 7.1:** Summary table of event selection criteria for different datasets.

| **Data sets** | $E_T^{miss}$**>=130** | **ΔR<=1** | Δ$\phi$, -2>phi<2 | $\eta$,-2>eta<2 | **M**>=70 | $HT$**>=880** |
|---|---|---|---|---|---|---|
| **Signal** | 1423.71 | 1393.91 | 1337.25 | 1280.59 | 1178.84 | 941.04 |
| **Background (ZZ)** | 6167.09 | 3676.65 | 3792.45 | 2456.21 | 2316 | 2229.49 |
| **Background (WW)** | 3811.94 | 1653.37 | 1377.81 | 1240.29 | 642.97 | 505.197 |
| **Background (tt~)** | 15780000 | 7320000 | 5640000 | 9192000 | 4056000 | 3888000 |

In second part of my thesis, I performed measurements using SQC setup at NCP for phase-2 upgrade. Within the CMS tracker, there are two sub detectors: the inner tracker and the outer tracker. In outer tracker, 2S modules are installed, which are silicon sensors measuring approximately $10 \times 10\,\mathrm{cm}^2$.

Each 2S sensor consists of 1016 parallel strips, segmented into two approximately 5 cm long strips, resulting in a total of 2032 channels. I measured eight parameters using specific equipment such as the LCR Meter, Source Measure unit (SMU), Electrometer, and Switch Matrix. Two of these parameters are referred to as global parameters, namely leakage current vs reverse bias voltage and bulk capacitance vs reverse bias voltage. The specified ranges for the global parameters of the 2S sensor can be found in Table 7.2.

**Table 7.2:** Acceptable ranges of strip parameters for 2S sensors.

| Electrical Parameters | Ranges |
|---|---|
| Full depletion voltage, $V_{\mathrm{fd}}$ | $< 350$ V |
| Current at 600 V, $I_{600}$ | 7.25 $\mu$A |
| Breakdown voltage, $V_{\mathrm{break}}$ | $> 800$ V |

The measured results of the global and strip parameters for the 2S sensor, batch 43264 are provided in Table 7.3 and 7.4. They are found to be within accepted range.

The remaining parameters, including coupling capacitance, inter-strip capacitance, strip current, poly-silicon resistance, inter-strip resistance, and dielectric current, are referred to as strip parameters.

**Table 7.3:** Measured average values of global parameters of the 2S sensor for batch 43264.

| Sensor No | $I$@600 (nA) | I @800 (nA) | I 800/I 600 (nA) | $V_{fd}$ |
|---|---|---|---|---|
| 38714_2S_019 | −130.87 | -138.39 | -1.057 | 228 |
| 38714_2S_023 | −122.17 | -129.87 | -1.063 | 228 |
| 38714_2S_037 | −170.27 | -180.69 | -1.061 | 228 |

| Sensor ID | Cc (pF) | $R_{\text{poly}}$ (MΩ) | $I_{\text{strip}}$ (pA) | $I_{\text{diel}}$ (pA) | $C_{\text{intl}}$ (pF) | $R_{\text{intl}}$ (GΩ) |
|---|---|---|---|---|---|---|
| NCP-43264-2S-35 | 142.9 | 1.54 | -39.7 | 0.37 | 1.62 | 209.8 |
| NCP-43264-2S-46 | 142.8 | 1.55 | -67.7 | 0.10 | 1.62 | 205.3 |
| NCP-43264-2S-49 | 143.1 | 1.51 | -63.1 | 0.39 | 1.62 | 191.7 |

**Table 7.4:** The average strip parameter values for batch 43264 of the 2S sensor.

# References


[1] SQC Specification document at NCP.

[2] Guido Altarelli. The Standard Model of particle physics. *arXiv preprint hep-ph/0510281*, 2005.

[3] Karim Laihem, Andreas Schälicke, S Riemann, and Andriy Ushakov. Study on low-energy positron polarimetry. Technical report, 2006.

[4] Francisco J Ynduráin. *The theory of quark and gluon interactions*. Springer Science & Business Media, 2007.

[5] Takele Kekeba Emana and Ethiopia Haramaya. Feynman diagrams of the Standard Model. 2017.

[6] Giorgio Apollinari, Lucio Rossi, and Oliver Brüning. High luminosity LHC project description. Technical report, 2014.

[7] Giorgio Apollinari, I Béjar Alonso, Oliver Brüning, M Lamont, and Lucio Rossi. High-luminosity Large Hadron Collider (HL-LHC): Preliminary design report. Technical report, Fermi National Accelerator Lab.(FNAL), Batavia, IL (United States), 2015.

[8] Marcin Andrzej Konecki. CMS performance, Physics, perspectives. *Acta Phys. Pol. B*, 45 (CMS-CR-2014-034):1427–1446, 2014.

[9] Serguei Chatrchyan, Lukas Bäni, Pierluigi Bortignon, Marco A Buchmann, Bruno Casal Laraña, Nicolas Chanon, Amanda Deisher, Günther Dissertori, Michael Dittmar, Mauro Donegà, et al. The performance of the CMS Muon detector in proton-proton collisions at s= 13.6 TeV at the LHC. *Journal of Instrumentation*, 8:P11002, 2013.

[10] Serguei Chatrchyan, EA de Wolf, P Van Mechelen, et al. The CMS experiment at the CERN LHC. *Journal of instrumentation.-Bristol, 2006, currens*, 3:S08004, 2008.

[11] Sally Seidel. Silicon strip and Pixel detectors for Particle Physics experiments. *Physics Reports*, 828:1–34, 2019.

[12] Philippe Bloch. Electromagnetic Calorimeter (ECAL). Technical report.

[13] J Freeman. Innovations for the CMS HCAL. *At the Leading Edge: The ATLAS and CMS LHC Experiments*, page 259, 2010.

[14] Gordon Kaußen. *Silicon strip detector qualification for the CMS experiment.* PhD thesis, Aachen, Tech. Hochsch., 2008.

[15] Alexander Dierlamm, CMS Tracker Collaboration, et al. The CMS outer tracker upgrade for the HL-LHC. *Nuclear Instruments and Methods in Physics Research Section A: Accelerators, Spectrometers, Detectors and Associated Equipment*, 924:256–261, 2019.

[16] Arabella Martelli. The CMS HGCAl detector for HL-LHC upgrade. *arXiv preprint arXiv:1708.08234*, 2017.

[17] F Bertola and Massimo Capaccioli. Dynamics of early type galaxies. i-the rotation curve of the elliptical galaxy NGC 4697. *Astrophysical Journal, vol. 200, Sept. 1, 1975, pt. 1, p. 439-445.*, 200:439–445, 1975.

[18] Harvey Tananbaum, MC Weisskopf, W Tucker, B Wilkes, and P Edmonds. Highlights and discoveries from the Chandra x-ray observatory. *Reports on Progress in Physics*, 77(6): 066902, 2014.

[19] Maxim Pospelov, Adam Ritz, and Mikhail Voloshin. Secluded WIMP Dark Matter. *Physics Letters B*, 662(1):53–61, 2008.

[20] Sanjoy Biswas, Emidio Gabrielli, Matti Heikinheimo, and Barbara Mele. Dark-photon searches via Higgs-boson production at the LHC. *Physical Review D*, 93(9):093011, 2016.

[21] Tomohiro Abe, Yoav Afik, Andreas Albert, Christopher R Anelli, Liron Barak, Martin Bauer, J Katharina Behr, Nicole F Bell, Antonio Boveia, Oleg Brandt, et al. LHC Dark Matter working group: Next-generation spin-0 Dark Matter Models. *Physics of the Dark Universe*, 27:100351, 2020.

[22] Ali Safa. *Characterisation of the new tracker Sensors for the CMS experiment at CERN.* PhD thesis, Brussels U., 2020.

[23] Thomas Bergauer, On behalf for the CMS Collaboration, et al. Silicon sensor prototypes for the phase II upgrade of the CMS tracker. *Nuclear Instruments and Methods in Physics Research Section A: Accelerators, Spectrometers, Detectors and Associated Equipment*, 831: 161–166, 2016.

[24] BC MacEvoy, K Gill, and G Hall. Defect-engineering rad-hard detectors for the CERN LHC. In *Materials Science Forum*, volume 258, pages 671–676. Trans Tech Publ, 1997.

[25] Kai Nordlund, Steven J Zinkle, Andrea E Sand, Fredric Granberg, Robert S Averback, Roger E Stoller, Tomoaki Suzudo, Lorenzo Malerba, Florian Banhart, William J Weber, et al. Primary radiation damage: A review of current understanding and models. *Journal of Nuclear Materials*, 512:450–479, 2018.

[26] FJ Grunthaner, BF Lewis, N Zamini, J Maserjian, and A Madhukar. Xps studies of structure-induced radiation effects at the Si/Sio2 interface. *IEEE Transactions on Nuclear Science*, 27(6):1640–1646, 1980.

[27] D Indumathi. Chien-shiung wu: The first lady of Physics. *Resonance*, 25(3):333–352, 2020.

[28] Antonio Dobado. Brout-Englert-Higgs mechanism for accelerating observers. *Physical Review D*, 96(8):085009, 2017.

[29] K Kodama, N Ushida, C Andreopoulos, N Saoulidou, G Tzanakos, P Yager, B Baller, D Boehnlein, W Freeman, B Lundberg, et al. Final tau-neutrino results from the DONUT experiment. *Physical Review D*, 78(5):052002, 2008.

[30] William Marciano and Heinz Pagels. Quantum chromodynamics. *Physics Reports*, 36(3): 137–276, 1978.

[31] Gregorio Bernardi and Matthew Herndon. Standard model Higgs boson searches through the 125 Gev boson discovery. *Reviews of Modern Physics*, 86(2):479, 2014.

[32] ATLAS collaboration et al. Muon reconstruction performance. ATLAS-CONF-2010-064, 2016.

[33] Antonella Palmese. *Unveiling the unseen with the Dark Energy Survey: Gravitational waves and Dark Matter*. PhD thesis, UCL (University College London), 2018.

[34] G Bellini, L Ludhova, G Ranucci, and FL Villante. Neutrino oscillations. *Advances in High Energy Physics*, 2014:1–28, 2014.

[35] Fritz Zwicky. On the theory and observation of highly collapsed stars. *Physical Review*, 55 (8):726, 1939.

[36] CS Kochanek, CR Keeton, and BA McLeod. The importance of Einstein rings. *The Astrophysical Journal*, 547(1):50, 2001.

[37] Gustavo Castelo Branco, PM Ferreira, L Lavoura, MN Rebelo, Marc Sher, and Joao P Silva. Theory and phenomenology of two-Higgs-Doublet models. *Physics reports*, 516(1-2): 1–102, 2012.

[38] Ilya F Ginzburg and Maria Krawczyk. Symmetries of two Higgs doublet model and C P violation. *Physical Review D*, 72(11):115013, 2005.

[39] Johan Alwall, Michel Herquet, Fabio Maltoni, Olivier Mattelaer, and Tim Stelzer. Madgraph 5: going beyond. *Journal of High Energy Physics*, 2011(6):1–40, 2011.

[40] Torbjörn Sjöstrand, Leif Lönnblad, Stephen Mrenna, and Peter Skands. PYTHIA 6.3. *arXiv preprint hep-ph/0308153*, 2003.

[41] ACAS Ravi Kumar and Arun Tripathi. Root: A data analysis and data mining tool from CERN. In *E-Forum Committee*, page 90.

[42] Henri Bachacou, Ian Hinchliffe, and Frank E Paige. Measurements of masses in supergravity Models at CERN LHC. *Physical Review D*, 62(1):015009, 2000.

[43] M Petasecca, F Moscatelli, Daniele Passeri, and GU Pignatel. Numerical simulation of radiation damage effects in p-type and n-type fz silicon detectors. *IEEE transactions on nuclear science*, 53(5):2971–2976, 2006.

[44] Kenneth G McKay. Avalanche breakdown in silicon. *Physical Review*, 94(4):877, 1954.

[45] Wim De Boer, Johannes Bol, Alex Furgeri, Steffen Müller, Christian Sander, Eleni Berdermann, Michal Pomorski, and Mika Huhtinen. Radiation hardness of diamond and Silicon Sensors compared. *physica status solidi (a)*, 204(9):3004–3010, 2007.